INTERNATIONAL JOURNAL FOR NUMERICAL METHODS IN ENGINEERING
Int. J. Numer. Meth. Engng 2003; **58**:1457–1497 (DOI: 10.1002/nme.819)

An accurate scheme for mixed-mode fracture analysis of functionally graded materials using the interaction integral and micromechanics models

Jeong-Ho Kim and Glaucio H. Paulino*,†

Department of Civil and Environmental Engineering, University of Illinois at Urbana-Champaign, Newmark Laboratory, 205 North Mathews Avenue, Urbana, IL 61801, U.S.A.

SUMMARY

The interaction integral is a conservation integral that relies on two admissible mechanical states for evaluating mixed-mode stress intensity factors (SIFs). The present paper extends this integral to functionally graded materials in which the material properties are determined by means of either continuum functions (e.g. exponentially graded materials) or micromechanics models (e.g. self-consistent, Mori–Tanaka, or three-phase model). In the latter case, there is no closed-form expression for the material-property variation, and thus several quantities, such as the explicit derivative of the strain energy density, need to be evaluated numerically (this leads to several implications in the numerical implementation). The SIFs are determined using conservation integrals involving known auxiliary solutions. The choice of such auxiliary fields and their implications on the solution procedure are discussed in detail. The computational implementation is done using the finite element method and thus the interaction energy contour integral is converted to an equivalent domain integral over a finite region surrounding the crack tip. Several examples are given which show that the proposed method is convenient, accurate, and computationally efficient. Copyright © 2003 John Wiley & Sons, Ltd.

KEY WORDS: functionally graded material; fracture mechanics; stress intensity factor; finite element method; interaction integral; conservation integral; micromechanics models

1. INTRODUCTION

The interaction integral method was developed for mixed-mode fracture analysis, and has been applied to homogeneous isotropic media [1], orthotropic solids [2] and bimaterial interface problems [3]. The method is based on conservation laws of elasticity and fracture mechanics concepts. The fundamental basis of the approach lies in the introduction of a conservation

*Correspondence to: Glaucio H. Paulino, Department of Civil and Environmental Engineering, University of Illinois at Urbana-Champaign, Newmark Laboratory, 205 North Mathews Avenue, Urbana, IL 61801, U.S.A.
†E-mail: paulino@uiuc.edu

Contract/grant sponsor: NASA-ames; contract/grant number: NAG 2-1424
Contract/grant sponsor: National Science Foundation; contract/grant number: CMS-0115954

Received 18 February 2002
Revised 2 January 2003
Accepted 10 January 2003

integral for two admissible states (actual and auxiliary fields) of an elastic solid. The analysis requires evaluation of the integral along a suitably selected path surrounding the crack tip (far-field).

In recent years, the interaction integral has emerged as a useful and viable technique to extract mixed-mode stress intensity factors (SIFs) in fracture mechanics problems. For example, the method has been used to determine mixed-mode SIFs along three-dimensional (3D) cracks in homogeneous materials [4, 5] and also in 3D bimaterial interface cracks considering straight [6] and curved cracks [7]. The same approach has been extended to through-cracks in Mindlin–Reissner plates by Dolbow *et al.* [8]. In the area of functionally graded materials (FGMs), the interaction integral method has been used with the extended finite element method (X-FEM) by Dolbow and Gosz [9], and with the element-free Galerkin (EFG) method by Rao and Rahman [10]. Both papers [9, 10] consider the material properties given by continuum functions (e.g. exponential or linear) and do not address micromechanics models.

Other methods have also been developed to investigate fracture of FGMs—see, for example, the review articles by Erdogan [11], Noda [12], Paulino *et al.* [13], and references therein. These include analytical or semi-analytical approaches such as those by Delale and Erdogan [14], Erdogan [11], Erdogan and Wu [15], and Chan *et al.* [16], who investigated various crack problems in FGMs with exponentially varying elastic modulus. Delale and Erdogan [17] have studied a crack in an FGM layer between two dissimilar homogeneous half-planes. Gu and Asaro [18] investigated a semi-infinite crack in an FGM strip. Shbeeb *et al.* [19, 20] have studied multiple cracks in an infinite nonhomogeneous plate. Honein and Herrmann [21] studied conservation laws in nonhomogeneous plane elastostatics and evaluated a semi-infinite crack by using the path-independent J_e-integral, which is obtained by means of a special version of Noether's theorem. The solutions obtained by these methods (i.e. analytical/semi-analytical) are used as benchmark results to validate the numerical methods in the present work.

Amongst the techniques used to investigate fracture of FGMs, the finite element method (FEM) has been one of the most popular methods. For mixed-mode crack problems, Eischen [22] has obtained mixed-mode SIFs in FGMs by means of the path-independent J_k^*-integral. Kim and Paulino [23] have also evaluated mixed-mode SIFs in FGMs by means of the path-independent J_k^*-integral using the equivalent domain integral (EDI) concept. For Mode I crack problems, Gu *et al.* [24] have presented a simplified method for evaluating SIFs using the standard J-integral. Anlas *et al.* [25] have calculated SIFs in FGMs by using the path-independent J_1^*-integral with element-wise homogeneous elastic properties. Marur and Tippur [26] have investigated a crack normal to the material gradient using the FEM in conjunction with experiments. Bao and Cai [27] have studied delamination cracking in a functionally graded ceramic/metal substrate under mechanical and thermal loads considering power-law type material gradation. Bao and Wang [28] have investigated periodic cracking in functionally graded ceramic/metal coatings under mechanical and thermal loads using the three-phase micromechanics model.

In an earlier paper published in this journal, we have used the FEM to evaluate mixed-mode SIFs in FGMs by means of the path-independent J_k^*-integral [23]. We have observed that the accuracy of J_k^*-integral is usually superior in mode I (involves J_1^*) than in mixed-mode (involves J_1^*, J_2^*) crack problems. This occurs essentially because the numerical treatment of crack faces which is needed to ensure path-independency of J_2^* may lead to loss of accuracy [23]. Moreover, both the theoretical formulation and numerical implementation for J_1^* are much simpler than for J_2^*. *From this point of view, a method that is based solely on*

the standard J-integral ($J = J_1 = J_1^*$) *for evaluating mixed-mode SIFs would be a highly attractive method. This is precisely the case with the interaction integral method* [1–3], *which is the main focus of this paper*. Here the interaction integral is implemented in a finite element framework and extended to evaluate mixed-mode SIFs in isotropic FGMs with material properties determined by means of either continuum functions (e.g. exponentially graded materials) or micromechanics models (e.g. self-consistent, Mori–Tanaka, or three-phase model). *Thus the contribution of this paper includes the interaction integral in conjunction with micromechanics models for FGMs.*

Because most of the present work focuses on SIFs obtained using micromechanics models for FGMs, a few remarks about such models are in order. The central assumption in applying classical micromechanics models to calculate effective properties of composites is the existence of a representative volume element (RVE) [29, 30]. However, the theoretical basis for such applications remains unclear because the concept of an RVE is not unique for FGMs in the presence of continuously changing properties due to non-uniform phase distribution [31]. To overcome such limitations, Aboudi *et al.* [31] have developed a higher-order micromechanical theory. Alternative approaches have been presented by Ostoja-Starzewski *et al.* [32] and Li [33]. Zuiker and Dvorak [34], Reiter *et al.* [35], Reiter and Dvorak [36], and Dvorak and Srinivas [37] have shown that, among various micromechanics models for conventional composite materials, the Mori–Tanaka and self-consistent models may be used to estimate the effective properties of graded materials with somewhat reasonable accuracy. Thus, in this work, we employ the Mori–Tanaka method (MT) [38], the self-consistent method (SCM) [39], and the three-phase model (TPM) [40], which is a generalized self-consistent model. Although these specific models are used in this work, *the methodology presented in this paper*, *using the interaction integral to evaluate SIFs in FGMs*, *is independent of the actual micromechanics model adopted and it can be used in conjunction with any micromechanics model.*

This paper is organized as follows. Section 2 presents auxiliary fields suitable for the interaction integral (called M-integral) method. Section 3 explains the M-integral formulation together with solution procedures and numerical aspects. Section 4 deals with the determination of material properties using both continuum models and micromechanics models. The *direct* and *indirect approaches* are used for evaluating quantities involving derivatives of material properties. The *direct approach* is associated with material properties given by closed form expressions (e.g. exponential material gradation), and the *indirect approach* is associated with effective material properties given by means of micromechanics models (no closed form expressions available). The direct approach includes the singular crack-tip elements and the indirect approach is implemented by either considering or neglecting the singular crack-tip elements. Section 5 presents various numerical examples in which the SIFs are evaluated by means of the M-integral. Finally, Section 6 presents some final remarks and conclusions.

2. AUXILIARY FIELDS

In order to apply the interaction integral to fracture mechanics, the auxiliary fields, such as stresses and displacements, are defined so that they involve SIFs. Figure 1 shows a crack in a two-dimensional FGM elastic body with applied tractions and displacements on the boundary. Local Cartesian and cylindrical co-ordinates originate from the crack tip. There are various

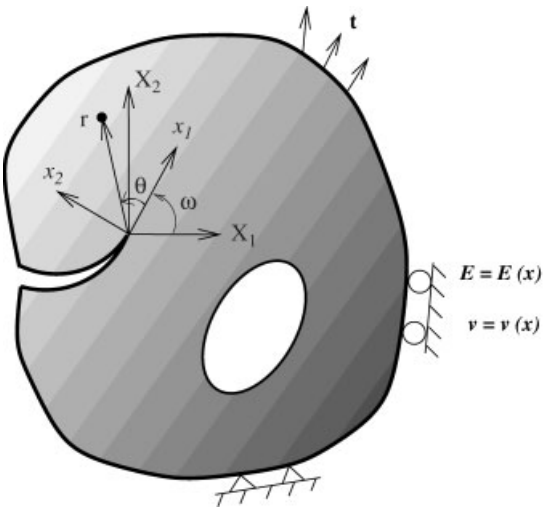

Figure 1. Co-ordinate systems at the crack tip.

suitable choices for the auxiliary fields. In this paper, we select the auxiliary fields as the crack-tip *asymptotic* fields, which coincide for both FGMs and homogeneous materials [22, 41, 42]. Notice, however, that the higher order terms do differ for FGMs and homogeneous materials [22, 43]. The auxiliary stress fields are chosen by neglecting the terms of $O(1)$ (so-called T-stress) and higher:

$$\sigma_{ij}^{\text{aux}} = \frac{K_{\text{I}}^{\text{aux}}}{\sqrt{2\pi r}} f_{ij}^{I}(\theta) + \frac{K_{\text{II}}^{\text{aux}}}{\sqrt{2\pi r}} f_{ij}^{\text{II}}(\theta), \quad (i,j=1,2) \tag{1}$$

and the corresponding auxiliary displacement fields are:

$$u_i^{\text{aux}} = \frac{K_{\text{I}}^{\text{aux}}}{\mu_{\text{tip}}} \sqrt{\frac{r}{2\pi}} g_i^{\text{I}}(\theta) + \frac{K_{\text{II}}^{\text{aux}}}{\mu_{\text{tip}}} \sqrt{\frac{r}{2\pi}} g_i^{\text{II}}(\theta), \quad (i=1,2) \tag{2}$$

where μ_{tip} is the shear modulus at the crack tip, and $K_{\text{I}}^{\text{aux}}$ and $K_{\text{II}}^{\text{aux}}$ are the auxiliary mode I and mode II SIFs, respectively. The standard angular functions $f_{ij}(\theta)$ and $g_i(\theta)$ $(i,j = 1,2)$ are given in many references, e.g. Reference [44]. Next, three alternative formulations to treat the auxiliary fields are discussed: incompatibility formulation, non-equilibrium formulation, and constant-constitutive-tensor formulation. The incompatibility and non-equilibrium formulations are equivalent to each other, and are the most accurate schemes. The constant-constitutive-tensor formulation involves derivatives of the actual stress field, which may introduce accuracy problems. Here we adopted the incompatibility formulation.

2.1. *Incompatibility formulation*

The auxiliary strain field is chosen as

$$\varepsilon_{ij}^{\text{aux}} = S_{ijkl}(\mathbf{x})\ \sigma_{kl}^{\text{aux}} \tag{3}$$

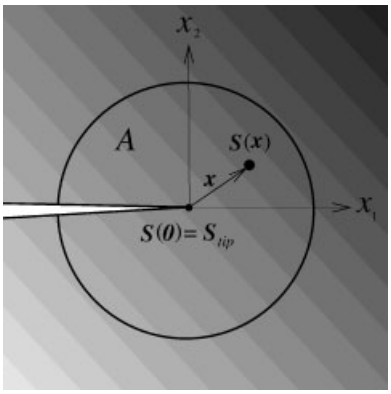

Figure 2. Illustration of the 'incompatibility formulation' accounting for material nonhomogeneity. Notice that, in general, $\mathbf{S}(\mathbf{x}) \neq \mathbf{S}_{\text{tip}}$ for $\mathbf{x} \neq \mathbf{0}$. The area A denotes a representative region around the crack tip.

where $S_{ijkl}(\mathbf{x})$ is the compliance tensor of FGMs and, in general, $S_{ijkl}(\mathbf{x}) \neq (S_{ijkl})_{\text{tip}}$ as shown in Figure 2. Notice that the auxiliary stress field in Equation (1) is in equilibrium, i.e. $\sigma^{\text{aux}}_{ij,j} = 0$ (no body forces), but the auxiliary strain field in Equation (3) is not compatible with the auxiliary displacement field in Equation (2), i.e. $\varepsilon^{\text{aux}}_{ij} \neq (u^{\text{aux}}_{i,j} + u^{\text{aux}}_{j,i})/2$. Thus such incompatibility has to be considered in the interaction integral formulation. The expression described above was proposed by Dolbow and Gosz [9], who applied it in conjunction with the extended FEM (X-FEM) to evaluate the interaction integral. It was also used by Rao and Rahman [10] (referred to as Method II in their paper), who applied it in conjunction with the element-free Galerkin (EFG) method. Here this technique is used in conjunction with the FEM, in which material properties are determined by means of either continuum functions or micromechanics models.

2.2. Non-equilibrium formulation

This method is the dual counterpart to the previous one, and the actual formulation is given by Kim and Paulino [45]. The auxiliary stress field is chosen as

$$\sigma^{\text{aux}}_{ij} = C_{ijkl}(\mathbf{x})\ \varepsilon^{\text{aux}}_{kl} \tag{4}$$

where $C_{ijkl}(\mathbf{x})$ is the spatially variable constitutive tensor (effective moduli), and $C^{-1}_{ijkl}(\mathbf{x}) = S_{ijkl}(\mathbf{x})$. Notice that the auxiliary stress field is not in equilibrium, i.e. $\sigma^{\text{aux}}_{ij,j} \neq 0$ (no body forces). In this case, the auxiliary displacement field is given by Equation (2), and the auxiliary strain field is the symmetric part of the gradient of the auxiliary displacement field, i.e. $\varepsilon^{\text{aux}}_{ij} = (u^{\text{aux}}_{i,j} + u^{\text{aux}}_{j,i})/2$. Therefore the auxiliary strain field is compatible with the auxiliary displacement field. This choice of the auxiliary fields has also been discussed by Dolbow and Gosz [9].

2.3. Constant-constitutive-tensor formulation

Another alternative for the auxiliary fields consists of choosing the auxiliary stress and displacement fields as given by Equations (1) and (2), respectively, and evaluating the auxiliary

strain fields by using the symmetric gradient of the auxiliary displacement fields. In this case, the stress-strain relationship is given by:

$$\sigma_{ij}^{\text{aux}} = (C_{ijkl})_{\text{tip}}\ \varepsilon_{ij}^{\text{aux}} \tag{5}$$

where $(C_{ijkl})_{\text{tip}}$ is a constant constitutive tensor evaluated at the crack tip. Notice that the constitutive relation is only satisfied at the crack tip location, and for other points around the crack tip $C_{ijkl}(\mathbf{x}) \neq (C_{ijkl})_{\text{tip}}$. Thus the greater the distance from the crack tip, the stronger the violation of the actual constitutive behaviour is. The auxiliary stress fields are in equilibrium and the auxiliary strain fields are compatible with the auxiliary displacement fields. This choice of the auxiliary fields has been discussed by Dolbow and Gosz [9] and implemented by Rao and Rahman [10] (referred to as Method I in their paper) using a meshless method. Their implementation [10] requires the derivatives of the actual stress field, which may have accuracy problems with standard C^0 elements commomly used in the displacement-based FEM.

3. THE INTERACTION INTEGRAL: M-INTEGRAL

The interaction integral (M-integral)[‡] is derived from the path-independent J-integral [49] for two admissible states of a cracked elastic FGM body. For the sake of numerical efficiency, the contour integral is transformed into an equivalent domain integral (EDI) [50]. First, the theoretical formulation is given, then the solution procedure and numerical aspects are discussed. Afterwards, the extraction of mixed-mode SIFs is presented.

3.1. M-integral: formulation

The path-independent J-integral [49] is defined as

$$J = \lim_{\Gamma_s \to 0} \int_{\Gamma_s} (\mathscr{W}\delta_{1j} - \sigma_{ij}u_{i,1})n_j \, \mathrm{d}\Gamma \tag{6}$$

where $\mathscr{W}$ is the strain energy density expressed by

$$\mathscr{W} = \tfrac{1}{2}\,\sigma_{ij}\varepsilon_{ij} = \tfrac{1}{2}\,C_{ijkl}\varepsilon_{kl}\varepsilon_{ij} \tag{7}$$

and n_j is the outward normal vector to the contour Γ_s, as shown in Figure 3. Let us define the following contour integral:

$$\mathscr{H} = \oint_{\Gamma} (\mathscr{W}\delta_{1j} - \sigma_{ij}u_{i,1})m_j q \, \mathrm{d}\Gamma \tag{8}$$

[‡]The present M-integral should not be confused with the conservation integral M of References [46–48].

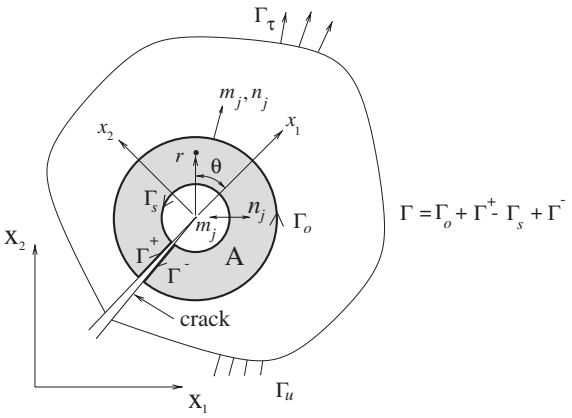

Figure 3. Conversion of the contour integral into an equivalent domain integral (EDI) where $\Gamma = \Gamma_o + \Gamma^+ - \Gamma_s + \Gamma^-$, $m_j = n_j$ on Γ_o and $m_j = -n_j$ on Γ_s.

where $\Gamma = \Gamma_o + \Gamma^+ - \Gamma_s + \Gamma^-$, m_j is a unit outward normal vector to the corresponding contour (i.e. $m_j = n_j$ on Γ_o and $m_j = -n_j$ on Γ_s), and q is a weight function defined as a smoothly varying function from $q = 1$ on Γ_s to $q = 0$ on Γ_o. Taking the limit $\Gamma_s \to 0$, one obtains

$$\lim_{\Gamma_s \to 0} \mathscr{H} = \lim_{\Gamma_s \to 0} \int_{\Gamma_o + \Gamma^+ + \Gamma^- - \Gamma_s} (\mathscr{W} \delta_{1j} - \sigma_{ij} u_{i,1}) m_j q \, \mathrm{d}\Gamma$$

$$= \lim_{\Gamma_s \to 0} \left[\int_{\Gamma_o + \Gamma^+ + \Gamma^-} (\mathscr{W} \delta_{1j} - \sigma_{ij} u_{i,1}) m_j q \, \mathrm{d}\Gamma - \int_{\Gamma_s} (\mathscr{W} \delta_{1j} - \sigma_{ij} u_{i,1}) n_j q \, \mathrm{d}\Gamma \right] \tag{9}$$

Because $q = 0$ on Γ_o and the crack faces are assumed to be traction-free, Equation (9) becomes

$$J = -\lim_{\Gamma_s \to 0} \mathscr{H} = -\lim_{\Gamma_s \to 0} \oint_{\Gamma} (\mathscr{W} \delta_{1j} - \sigma_{ij} u_{i,1}) m_j q \, \mathrm{d}\Gamma \tag{10}$$

Applying the divergence theorem and using the weight function q, one obtains the following EDI:

$$J = \int_A (\sigma_{ij} \; u_{i,1} - \mathscr{W} \delta_{1j})_{,j} q \, \mathrm{d}A + \int_A (\sigma_{ij} u_{i,1} - \mathscr{W} \delta_{1j}) q_{,j} \, \mathrm{d}A \tag{11}$$

where q varies from unity at the crack tip to zero along the outer contour. Here the plateau q-function is used, which can be found in many references, e.g. References [51, 52]. Let us define the first integral of Equation (11) as I, i.e.

$$I = \int_A (\sigma_{ij} u_{i,1} - \mathscr{W} \delta_{1j})_{,j} q \, \mathrm{d}A = \int_A (\sigma_{ij,j} \; u_{i,1} + \sigma_{ij} u_{i,1j} - \mathscr{W}_{,1}) q \, \mathrm{d}A \tag{12}$$

The derivative of the strain energy density (with respect to the local crack system) is obtained as

$$\mathscr{W}_{,1} = \frac{\partial \mathscr{W}}{\partial x_1} = \sigma_{ij}\varepsilon_{ij,1} + \tfrac{1}{2}\, C_{ijkl,1}\varepsilon_{kl}\varepsilon_{ij} \tag{13}$$

where $C_{ijkl} = C_{ijkl}(\mathbf{x})$ is the FGM constitutive tensor. Substituting the last expression of Equation (13) into Equation (12), one obtains

$$I = \int_A \left\{ \underline{\sigma_{ij}(u_{i,1j} - \varepsilon_{ij,1})} - \tfrac{1}{2}\, C_{ijkl,1}\varepsilon_{kl}\varepsilon_{ij} \right\} q \, \mathrm{d}A \tag{14}$$

in the absence of body forces, i.e. $\sigma_{ij,j} = 0$. Although the actual fields satisfy $\sigma_{ij}\varepsilon_{ij,1} = \sigma_{ij}u_{i,1j}$, we do not cancel out the terms underlined in Equation (14) but keep them through the derivation of the M-integral. This derivation is based on the work by Dolbow and Gosz [9], and it is done in order to anticipate the incompatiblity of the auxiliary strain field with the auxiliary displacement field, which will be discussed later. Substitution of Equation (14) into Equation (11) yields

$$J = \int_A (\sigma_{ij}u_{i,1} - \mathscr{W}\delta_{1j})q_{,j} \, \mathrm{d}A + \int_A \left\{ \sigma_{ij}(u_{i,1j} - \varepsilon_{ij,1}) - \tfrac{1}{2}\, C_{ijkl,1}\varepsilon_{kl}\varepsilon_{ij} \right\} q \, \mathrm{d}A \tag{15}$$

Let us now consider two independent admissible fields which are the actual $(\mathbf{u}, \boldsymbol{\varepsilon}, \boldsymbol{\sigma})$ and auxiliary $(\mathbf{u}^{\mathrm{aux}}, \boldsymbol{\varepsilon}^{\mathrm{aux}}, \boldsymbol{\sigma}^{\mathrm{aux}})$ fields. The J-integral of the superimposed fields (actual and auxiliary) can be written as:

$$\begin{aligned} J^s = & \int_A \left\{ (\sigma_{ij} + \sigma_{ij}^{\mathrm{aux}})(u_{i,1} + u_{i,1}^{\mathrm{aux}}) - \tfrac{1}{2}\,(\sigma_{ik} + \sigma_{ik}^{\mathrm{aux}})(\varepsilon_{ik} + \varepsilon_{ik}^{\mathrm{aux}})\delta_{1j} \right\} q_{,j} \, \mathrm{d}A \\ & + \int_A \left\{ (\sigma_{ij} + \sigma_{ij}^{\mathrm{aux}})(u_{i,1j} - \varepsilon_{ij,1} + u_{i,1j}^{\mathrm{aux}} - \varepsilon_{ij,1}^{\mathrm{aux}}) \right. \\ & \left. - \tfrac{1}{2}\, C_{ijkl,1}(\varepsilon_{kl} + \varepsilon_{kl}^{\mathrm{aux}})(\varepsilon_{ij} + \varepsilon_{ij}^{\mathrm{aux}}) \right\} q \, \mathrm{d}A \end{aligned} \tag{16}$$

and can be conveniently decomposed into

$$J^s = J + J^{\mathrm{aux}} + M \tag{17}$$

where J is given by Equation (15), J^{aux} is given by

$$J^{\mathrm{aux}} = \int_A (\sigma_{ij}^{\mathrm{aux}}u_{i,1}^{\mathrm{aux}} - \mathscr{W}^{\mathrm{aux}}\delta_{1j})q_{,j} \, \mathrm{d}A + \int_A \left\{ \sigma_{ij}^{\mathrm{aux}}(u_{i,1j}^{\mathrm{aux}} - \varepsilon_{ij,1}^{\mathrm{aux}}) - \tfrac{1}{2}\, C_{ijkl,1}\varepsilon_{kl}^{\mathrm{aux}}\varepsilon_{ij}^{\mathrm{aux}} \right\} q \, \mathrm{d}A \tag{18}$$

which is analogous to Equation (15) with

$$\mathscr{W}^{\mathrm{aux}} = \tfrac{1}{2}\, \sigma_{ij}^{\mathrm{aux}}\varepsilon_{ij}^{\mathrm{aux}} = \tfrac{1}{2}\, C_{ijkl}\varepsilon_{kl}^{\mathrm{aux}}\varepsilon_{ij}^{\mathrm{aux}} \tag{19}$$

and M is the interaction integral (involving both actual and auxiliary fields) given by

$$M = \int_A \left\{ (\sigma_{ij} u^{\text{aux}}_{i,1} + \sigma^{\text{aux}}_{ij} u_{i,1}) - \tfrac{1}{2} (\sigma_{ik} \varepsilon^{\text{aux}}_{ik} + \sigma^{\text{aux}}_{ik} \varepsilon_{ik}) \delta_{1j} \right\} q_{,j} \, \mathrm{d}A$$
$$+ \int_A \left\{ (\sigma_{ij} (u^{\text{aux}}_{i,1j} - \varepsilon^{\text{aux}}_{ij,1}) + \sigma^{\text{aux}}_{ij} (u_{i,1j} - \varepsilon_{ij,1}) - \tfrac{1}{2} C_{ijkl,1} (\varepsilon_{ij} \varepsilon^{\text{aux}}_{kl} + \varepsilon^{\text{aux}}_{ij} \varepsilon_{kl}) \right\} q \, \mathrm{d}A \tag{20}$$

Because

$$\begin{gathered} \sigma^{\text{aux}}_{ij} u_{i,1j} = \sigma^{\text{aux}}_{ij} \varepsilon_{ij,1} \\ \sigma_{ij} \varepsilon^{\text{aux}}_{ij} = C_{ijkl} \varepsilon_{kl} \varepsilon^{\text{aux}}_{ij} = C_{klij} \varepsilon^{\text{aux}}_{ij} \varepsilon_{kl} = \sigma^{\text{aux}}_{kl} \varepsilon_{kl} = \sigma^{\text{aux}}_{ij} \varepsilon_{ij} \\ C_{ijkl,1} \varepsilon^{\text{aux}}_{ij} \varepsilon_{kl} = C_{ijkl,1} \varepsilon_{ij} \varepsilon^{\text{aux}}_{kl} \end{gathered} \tag{21}$$

then Equation (20) becomes

$$M = \int_A \left\{ \sigma_{ij} u^{\text{aux}}_{i,1} + \sigma^{\text{aux}}_{ij} u_{i,1} - \sigma_{ik} \varepsilon^{\text{aux}}_{ik} \delta_{1j} \right\} q_{,j} \, \mathrm{d}A + \int_A \left\{ \underline{\sigma_{ij} (u^{\text{aux}}_{i,1j} - \varepsilon^{\text{aux}}_{ij,1})} - C_{ijkl,1} \varepsilon_{ij} \varepsilon^{\text{aux}}_{kl} \right\} q \, \mathrm{d}A \tag{22}$$

which is the interaction integral involving the actual and auxiliary fields. Notice that the incompatiblity terms, underlined in Equation (22), arise naturally in the M-integral formulation.

3.2. *M-integral: solution procedure and numerical aspects*

Since the FEM computation of displacements, strains, stresses, etc., is based on the global co-ordinate system, the M-integral is evaluated first in the global co-ordinate system (M_{global}) and then transformed to the local system (M_{local}). Equation (22) can be recast in the following form ($m = 1, 2$):

$$(M_m)_{\text{local}} = \int_A \{ \sigma_{ij} u^{\text{aux}}_{i,m} + \sigma^{\text{aux}}_{ij} u_{i,m} - \sigma_{ik} \varepsilon^{\text{aux}}_{ik} \delta_{mj} \} \frac{\partial q}{\partial x_j} \, \mathrm{d}A + \int_A \{ \underline{\sigma_{ij} (u^{\text{aux}}_{i,mj} - \varepsilon^{\text{aux}}_{ij,m})} - C_{ijkl,m} \varepsilon_{ij} \varepsilon^{\text{aux}}_{kl} \} q \, \mathrm{d}A \tag{23}$$

where the underlined terms indicate the extra incompatiblity terms which arise in the formulation. Thus for $m = 1$, $(M)_{\text{local}} = (M_1)_{\text{local}}$. The above expressions are represented by the local co-ordinates x_i, which can be expressed in terms of the global co-ordinates X_i by the co-ordinate transformation $x_i = \alpha_{ij}(\theta) X_j$, where $\alpha_{ij}(\theta)$ is the standard co-ordinate transformation matrix. The same transformation also holds for the M-integral, and thus ($i, j = 1, 2$)

$$(M_i)_{\text{local}} = \alpha_{ij}(\theta) (M_i)_{\text{global}}, \quad \alpha_{ij}(\theta) = \begin{bmatrix} \cos\theta & \sin\theta \\ -\sin\theta & \cos\theta \end{bmatrix} \tag{24}$$

For the sake of numerical implementation by the FEM, Equation (23) is evaluated in global co-ordinates. Therefore $(m=1,2)$

$$(M_m)_{\text{global}} = \int_A \{\sigma_{ij} u^{\text{aux}}_{i,m} + \sigma^{\text{aux}}_{ij} u_{i,m} - \sigma_{ik}\varepsilon^{\text{aux}}_{ik}\delta_{mj}\} \frac{\partial q}{\partial X_j}\, \mathrm{d}A + \int_A \{\underline{\sigma_{ij}(u^{\text{aux}}_{i,mj} - \varepsilon^{\text{aux}}_{ij,m})} - C_{ijkl,m}\varepsilon_{ij}\varepsilon^{\text{aux}}_{kl}\} q\, \mathrm{d}A \tag{25}$$

The derivatives of the auxiliary strain fields (due to incompatibility) in Equation (25) must be carefully evaluated, as explained in Appendix A. The defined quantities $(M_1)_{\text{global}}$ and $(M_2)_{\text{global}}$ in Equation (25) are computed in order to calculate M_{local} according to the transformation given by Equation (24), i.e.

$$M_{\text{local}} = (M_1)_{\text{local}} = (M_1)_{\text{global}} \cos\theta + (M_2)_{\text{global}} \sin\theta \tag{26}$$

3.3. *M-integral: stress intensity factors*

The relationship among J-integral and the mode I and mode II stress intensity factors is established as:

$$J_{\text{local}} = \frac{K_{\text{I}}^2 + K_{\text{II}}^2}{E'_{\text{tip}}} \tag{27}$$

where

$$E'_{\text{tip}} = \begin{cases} E_{\text{tip}} & \text{generalized plane stress} \\ E_{\text{tip}}/(1-\nu^2_{\text{tip}}) & \text{plane strain} \end{cases} \tag{28}$$

By superimposing the actual and auxiliary fields, and using Equation (27), one obtains

$$J^s_{\text{local}} = \frac{(K_{\text{I}} + K^{\text{aux}}_{\text{I}})^2 + (K_{\text{II}} + K^{\text{aux}}_{\text{II}})^2}{E'_{\text{tip}}} \tag{29}$$

$$= J^{\text{aux}}_{\text{local}} + J_{\text{local}} + M_{\text{local}} \tag{30}$$

where

$$J^{\text{aux}}_{\text{local}} = \frac{(K^{\text{aux}}_{\text{I}})^2 + (K^{\text{aux}}_{\text{II}})^2}{E'_{\text{tip}}} \tag{31}$$

and

$$M_{\text{local}} = \frac{2}{E'_{\text{tip}}} (K_{\text{I}} K^{\text{aux}}_{\text{I}} + K_{\text{II}} K^{\text{aux}}_{\text{II}}) \tag{32}$$

The mode I stress intensity factor (K_{I}) can be computed by setting $K^{\text{aux}}_{\text{I}} = 1.0$ and $K^{\text{aux}}_{\text{II}} = 0.0$, i.e.

$$K_{\text{I}} = \frac{E'_{\text{tip}}}{2} M^{(1)}_{\text{local}} \tag{33}$$

Similarly, the mode II stress intensity factor (K_{II}) can be obtained by setting $K_{\mathrm{I}}^{\mathrm{aux}} = 0.0$ and $K_{\mathrm{II}}^{\mathrm{aux}} = 1.0$, i.e.

$$K_{\mathrm{II}} = \frac{E'_{\mathrm{tip}}}{2} M_{\mathrm{local}}^{(2)} \tag{34}$$

Relationships (33) and (34) are essentially the same as those by Yau *et al.* [1], the only difference being that, for the FGM case, the material properties are evaluated at the crack-tip location.

4. MATERIAL PROPERTIES

The model used to evaluate material properties has major implications on the implementation of the interaction integral (M-integral). According to Table I, both *direct* and *indirect* approaches are used for evaluating quantities involving derivatives of material properties. The *direct approach* is associated with material properties given by closed form expressions (e.g. exponential material gradation), while the *indirect approach* is associated with effective material properties obtained by means of micromechanics models. In the latter case, there are no closed form expressions for the material property variation. The direct approach includes the singular crack-tip elements. The indirect approach is implemented by either neglecting or considering the crack-tip elements, as illustrated by Figure 4. The motivation for this comparison is to show the influence of the singular crack-tip elements on the solution. By neglecting the crack-tip elements, an exclusion region is introduced at the stage of post-processing the finite element solution to evaluate fracture parameters (e.g. SIFs). Exclusion of the crack-tip elements was also considered by Raju and Shivakumar [50] to solve 2D mixed-mode crack problems.

4.1. Continuum models

For the so-called continuum models with known functions of material properties (e.g. exponential gradation or linear gradation), the M-integral can be evaluated directly by using Equation (23). This constitutes the so called *direct approach* (see Table I). For instance, consider the general case of an exponentially graded material in which the material gradation can

Table I. Material property evaluation.

	Derivatives	
Approach	Direct	Indirect
Material	Continuum functions	Micromechanics models
Crack-tip elements	Included	Included Excluded

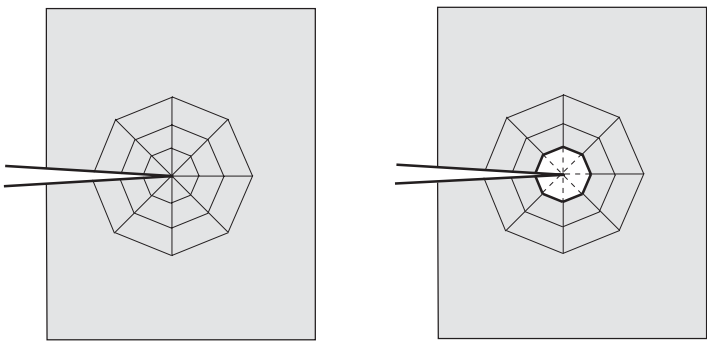

Figure 4. Illustration of the domain used in the 'Indirect approach' to evaluate SIFs by the conservative M-integral: (a) including crack-tip elements; and (b) excluding crack-tip elements.

vary in any direction and is characterized by the nonhomogeneity parameters β_1 and β_2, i.e.

$$E(x_1) = E_0 \exp(\beta_1 X_1 + \beta_2 X_2) \tag{35}$$

The derivatives of interest, with respect to the global co-ordinate system (X_j), are $(m = 1, 2)$

$$\begin{aligned} C_{ijkl,m} &= \beta_m C_{ijkl} \\ \varepsilon^{\text{aux}}_{ij,m} &= S_{ijkl,m}\sigma^{\text{aux}}_{kl} + S_{ijkl}\sigma^{\text{aux}}_{kl,m} \\ &= -\beta_m S_{ijkl}\sigma^{\text{aux}}_{kl} + S_{ijkl}\sigma^{\text{aux}}_{kl,m} \end{aligned} \tag{36}$$

Substitution of Equation (36) into Equation (25) yields $(m = 1, 2)$

$$(M_m)_{\text{global}} = \int_A \{\sigma_{ij} u^{\text{aux}}_{i,m} + \sigma^{\text{aux}}_{ij} u_{i,m} - \sigma_{ik}\varepsilon^{\text{aux}}_{ik}\delta_{mj}\} \frac{\partial q}{\partial X_j}\, \mathrm{d}A + \int_A \{\sigma_{ij} u^{\text{aux}}_{i,mj} - \sigma^{\text{aux}}_{ij,m}\varepsilon_{ij}\} q\, \mathrm{d}A \tag{37}$$

where the second identity in Equation (21) has also been used to simplify the above expression.

4.2. *Micromechanics models extended to FGMs*

The effective material properties in FGMs, which usually possess large variations in volume fractions of the constituent materials, can (arguably) be predicted over the entire range of volume fractions (e.g. $0.0 \leqslant V_f \leqslant 1.0$) by extending existing *micromechanics models*. In this case, special consideration should be taken for implementing the M-integral, especially in dealing with derivatives of material properties.

For two-phase FGMs, the volume fraction is assumed here in the form of a power function, i.e.

$$V_i(X) = (X/L)^p \tag{38}$$

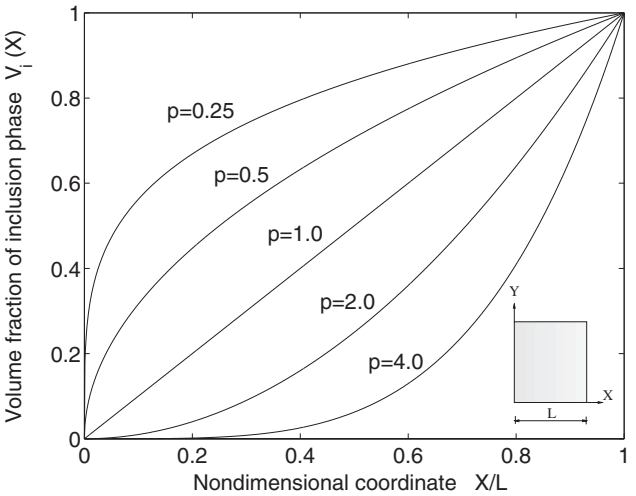

Figure 5. Volume fractions of the inclusion phase.

where the subscript i stands for the 'inclusion phase', and L is the material gradation length. Thus $X = 0$ corresponds to pure matrix phase and $X = L$ to pure inclusion material. Figure 5 shows the volume fraction of the inclusion phase for various values of p. The exponent p dictates the nature of the desired distribution function. For example, in FGMs of TiC/Ni, the optimum value for p was reported to be in the range $[0.5 - 0.7]$ [53].

The volume fraction of the material constituents may or may not be represented by explicit functions such as the one in Equation (38). Thus we evaluate material properties by using *discrete* values of the volume fraction. Moreover, here we do not use closed-form expressions to evaluate derivatives of material properties because these expressions would be specific to each specific micromechanics model. Thus, for the sake of generality, we determine derivatives of material properties by using shape function derivatives of finite elements [23, 62].

4.2.1. Selected micromechanics models. Various micromechanics models can be applied to predict the effective elastic properties of FGMs, either based on classical approaches [54] or alternative ones [31]. As motivated in the introduction of this paper, in this work we investigate the self-consistent method [39, 55–57], the three phase model [40], and the Mori–Tanaka method [38]. These specific models are considered, as well as the Hashin–Shtrikman bounds [58], which provide practical, closely spaced bounds on the elastic moduli of composite materials. For FGMs, these models are evaluated as many times as needed by considering the range of interest of the volume fraction of the constituent materials.

• *Hashin–Shtrikman Bounds*

Hashin and Shtrikman [58] derived upper and lower bounds for the effective elastic moduli of multiphase materials, consisting of isotropic phases, by means of variational principles for non-homogeneous and isotropic elasticity in the case of prescribed surface displacements.

For two-phase materials, the bounds on the effective shear and bulk moduli are [58] $(i, j = 1, 2)$:

$$\mu_i^e = \mu_i + V_j \Big/ \left\{ \frac{1}{\mu_j - \mu_i} + \frac{6(\kappa_i + 2\mu_i)V_i}{5\mu_i(3\kappa_i + 4\mu_i)} \right\}$$
$$\kappa_i^e = \kappa_i + V_j \Big/ \left\{ \frac{1}{\kappa_j - \kappa_i} + \frac{3V_i}{(3\kappa_i + 4\mu_i)} \right\}, \quad (i \neq j) \tag{39}$$

where the superscript e refers to the effective quantity, V_i is the volume fraction of phase i, μ_i is the shear modulus of phase i, and κ_i is the bulk modulus of phase i. Moreover, $\kappa_2^e > \kappa_1^e$ and $\mu_2^e > \mu_1^e$.

• *Self-consistent method* (SCM)

The self-consistent method was derived as a means to model the behaviour of single-phase polycrystalline materials, but because of the random or partially random orientation of the crystals, discontinuities in properties exist across crystal interfaces. In the application to polycrystalline aggregates, a single anisotropic crystal is viewed as a spherical or ellipsoidal inclusion embedded in an infinite medium with the unknown isotropic properties of the aggregate. Then the system is subjected to uniform stress or strain conditions at large distances from the inclusion. Next the orientation average of the stress or strain in the inclusion is set equal to the corresponding applied value of the stress or strain, hence the name 'self-consistent' for this procedure.

For a two-phase composite, the shear and bulk moduli (μ, κ) are given as [39]

$$\frac{1}{\kappa + 4\mu/3} = \frac{V_1}{\kappa_1 + 4\mu/3} + \frac{V_2}{\kappa_2 + 4\mu/3} \tag{40}$$

$$\left(\frac{V_1\kappa_1}{\kappa_1 + 4\mu/3} + \frac{V_2\kappa_2}{\kappa_2 + 4\mu/3} \right) + 5 \left(\frac{V_1\mu_2}{\mu - \mu_2} + \frac{V_2\mu_1}{\mu - \mu_1} \right) + 2 = 0 \tag{41}$$

where V_1 and V_2 are the volume fractions of phases 1 and 2, respectively. After the above equations are solved locally for μ and κ, the Young's modulus E and the Poisson's ratio v of the composite are obtained as

$$E = \frac{9\mu\kappa}{\mu + 3\kappa}, \quad v = \frac{3\kappa - 2\mu}{2(\mu + 3\kappa)} \tag{42}$$

• *Three phase model* (TPM)

The three phase model is also referred to as the *generalized self-consistent method* because it follows from the original self-consistent method, which involves directly embedding the inclusion phase in the infinite medium of unknown effective properties.

The final solution for shear modulus μ is obtained by solving the following quadratic equation [40]:

$$A(\mu/\mu_1)^2 + 2B(\mu/\mu_1) + C = 0 \tag{43}$$

where the constants A, B, and C are given in Reference [40] in terms of the material properties of the inclusion (μ_1, ν_1) and matrix (μ_2, ν_2) phases, and the volume fraction of the inclusion (V_2). The solution for the effective bulk modulus is given by

$$\kappa = \kappa_1 + V_2(\kappa_2 - \kappa_1) \Big/ \left[1 + V_1 \left\{ \frac{\kappa_2 - \kappa_1}{\kappa_1 + 4\mu_1/3} \right\}\right] \tag{44}$$

As before, the Young's modulus E and the Poisson's ratio ν of the composite are obtained using Equation (42).

• *Mori–Tanaka Method* (MT)
Like the self-consistent method, the Mori–Tanaka method also uses the average local stress and strain fields of the constituents of the composite to estimate the effective material properties. However, the key to the Mori–Tanaka method is essentially mathematical and involves average strain, average stress, and concentration tensors for dilute and non-dilute conditions. The Mori–Tanaka method when applied to the spherical inclusion problem under non-dilute conditions yields [38]:

$$\mu = \mu_1 + V_2(\mu_2 - \mu_1) \Big/ \left[1 + V_1 \left\{ \frac{\mu_2 - \mu_1}{\mu_1 + \dfrac{\mu_1(9\kappa_1 + 8\mu_1)}{6(\kappa_1 + 2\mu_1)}} \right\}\right] \tag{45}$$

$$\kappa = \kappa_1 + V_2(\kappa_2 - \kappa_1) \Big/ \left[1 + V_1 \left\{ \frac{\kappa_2 - \kappa_1}{\kappa_1 + 4\mu_1/3} \right\}\right] \tag{46}$$

Again, the Young's modulus E and the Poisson's ratio ν of the composite are obtained using Equation (42).

4.2.2. M-integral implementation for regular elements. When micromechanics models are used, there is no closed form expression available for the effective material properties (as in Section 4.1). The *indirect approach*, which is associated with micromechanics models, is implemented by either neglecting or considering the crack-tip elements (cf. Table I and Figure 4). In both cases, the following form of the M-integral is used for *regular elements* (i.e. non-singular), which is derived from Equation (22):

$$\begin{aligned} M = (M_1)_{\text{local}} &= \int_A (\sigma_{ij} u^{\text{aux}}_{i,1} + \sigma^{\text{aux}}_{ij} u_{i,1} - \sigma_{\text{st}} \varepsilon^{\text{aux}}_{\text{st}} \delta_{1j}) \frac{\partial q}{\partial x_j} \, \mathrm{d}A \\ &\quad + \int_A (\sigma_{ij} u^{\text{aux}}_{i,1} + \sigma^{\text{aux}}_{ij} u_{i,1} - \sigma_{\text{st}} \varepsilon^{\text{aux}}_{\text{st}} \delta_{1j})_{,j} q \, \mathrm{d}A \\ &= \int_A (\sigma_{ij} u^{\text{aux}}_{i,1} + \sigma^{\text{aux}}_{ij} u_{i,1} - \sigma_{\text{st}} \varepsilon^{\text{aux}}_{\text{st}} \delta_{1j}) \frac{\partial q}{\partial x_j} \, \mathrm{d}A \\ &\quad - \int_A (\sigma_{\text{st},1} \varepsilon^{\text{aux}}_{\text{st}} + \sigma_{\text{st}} \varepsilon^{\text{aux}}_{\text{st},1}) q \, \mathrm{d}A + \int_A (\sigma_{ij} u^{\text{aux}}_{i,1j} + \sigma^{\text{aux}}_{ij} u_{i,1j}) q \, \mathrm{d}A \end{aligned} \tag{47}$$

As explained in Section 3.2, the numerical implementation (FEM) of the M-integral is done in global co-ordinates ($m=1,2$)

$$(M_m)_{\text{global}} = \int_A (\sigma_{ij} u^{\text{aux}}_{i,m} + \sigma^{\text{aux}}_{ij} u_{i,m} - \sigma_{\text{st}} \varepsilon^{\text{aux}}_{\text{st}} \delta_{mj}) \frac{\partial q}{\partial X_j} \, \mathrm{d}A - \int_A (\sigma_{\text{st},m} \varepsilon^{\text{aux}}_{\text{st}} + \sigma_{\text{st}} \varepsilon^{\text{aux}}_{\text{st},m}) q \, \mathrm{d}A + \int_A (\sigma_{ij} u^{\text{aux}}_{i,mj} + \sigma^{\text{aux}}_{ij} u_{i,mj}) q \, \mathrm{d}A \tag{48}$$

and then transformed to the local system according to Equation (26). Notice that the quantities $u^{\text{aux}}_{i,m}$, σ^{aux}_{ij}, $\varepsilon^{\text{aux}}_{ij}$, and $u^{\text{aux}}_{i,mj}$ do not involve derivatives of the spatially varying constitutive tensor, so these auxiliary quantities can be evaluated analytically. However, the quantity $\varepsilon^{\text{aux}}_{\text{st},m}$ does involve its derivatives, and is numerically calculated. One of the ways to evaluate $\varepsilon^{\text{aux}}_{\text{st},m}$ is to use shape function derivatives and Gauss-point quantities of the auxiliary strain fields $\varepsilon^{\text{aux}}_{\text{st}}$. This is illustrated below for both Q8 and T6 elements, but the procedure is also valid for other element types.

For Q8 elements [50],

$$\varepsilon^{\text{aux}}_{\text{st}}(\xi,\eta) = a_1 + a_2\xi + a_3\eta + a_4\xi\eta \tag{49}$$

where ξ and η are natural co-ordinates. Using 2×2 Gaussian quantities of the auxiliary strain fields, one writes $\varepsilon^{\text{aux}}_{\text{st}}$ as

$$\varepsilon^{\text{aux}}_{\text{st}}(\xi,\eta) = [1 \;\; \xi \;\; \eta \;\; \xi\eta] \;\; \mathbf{T} \;\; \varepsilon^{\text{aux}}_{\text{st}(G)} \tag{50}$$

where

$$\mathbf{T} = \frac{1}{4} \begin{bmatrix} 1 & 1 & 1 & 1 \\ -\sqrt{3} & \sqrt{3} & -\sqrt{3} & \sqrt{3} \\ \sqrt{3} & \sqrt{3} & -\sqrt{3} & -\sqrt{3} \\ -3 & 3 & 3 & -3 \end{bmatrix} \tag{51}$$

and

$$[\varepsilon^{\text{aux}}_{\text{st}(G)}]^{\text{T}} = [\varepsilon^{\text{aux}}_{\text{st}(G1)} \;\; \varepsilon^{\text{aux}}_{\text{st}(G2)} \;\; \varepsilon^{\text{aux}}_{\text{st}(G3)} \;\; \varepsilon^{\text{aux}}_{\text{st}(G4)}]^{\text{T}} \tag{52}$$

in which $\varepsilon^{\text{aux}}_{\text{st}(G1)}$, $\varepsilon^{\text{aux}}_{\text{st}(G2)}$, $\varepsilon^{\text{aux}}_{\text{st}(G3)}$, and $\varepsilon^{\text{aux}}_{\text{st}(G4)}$ are the auxiliary strain values at the Gaussian points as shown in Figure 6(a). The partial derivatives $\partial\varepsilon^{\text{aux}}_{\text{st}}/\partial\xi$ and $\partial\varepsilon^{\text{aux}}_{\text{st}}/\partial\eta$ are

$$\begin{Bmatrix} \partial\varepsilon^{\text{aux}}_{\text{st}}/\partial\xi \\ \partial\varepsilon^{\text{aux}}_{\text{st}}/\partial\eta \end{Bmatrix} = \begin{bmatrix} 0 & 1 & 0 & \eta \\ 0 & 0 & 1 & \xi \end{bmatrix} \;\; \mathbf{T} \;\; \varepsilon^{\text{aux}}_{\text{st}(G)} \tag{53}$$

Then the derivatives $\partial\varepsilon^{\text{aux}}_{\text{st}}/\partial X_m$ ($m=1,2$) can be readily obtained as

$$\begin{Bmatrix} \partial\varepsilon^{\text{aux}}_{\text{st}}/\partial X_1 \\ \partial\varepsilon^{\text{aux}}_{\text{st}}/\partial X_2 \end{Bmatrix} = \mathbf{J}^{-1} \begin{Bmatrix} \partial\varepsilon^{\text{aux}}_{\text{st}}/\partial\xi \\ \partial\varepsilon^{\text{aux}}_{\text{st}}/\partial\eta \end{Bmatrix} \tag{54}$$

where $\mathbf{J}^{-1}$ is the inverse of the Jacobian matrix.

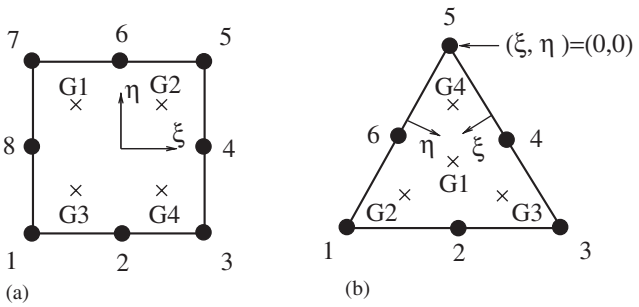

Figure 6. Gaussian quadrature: (a) Q8 element (2×2); and (b) T6 element (4 point). Nodes are numbered counter-clockwise.

Similarly, for T6 elements,

$$\varepsilon_{st}^{aux}(\xi,\eta) = b_1 + b_2\xi + b_3\eta + b_4\xi\eta \tag{55}$$

where ξ and η are triangular natural co-ordinates. Using four Gauss sampling points as shown in Figure 6(b), one uses Equation (50) with the matrix $\mathbf{T}$ given by

$$\mathbf{T} = \frac{1}{4}\begin{bmatrix} 9 & -5 & -5 & 5 \\ -45 & 25 & 15 & 5 \\ -45 & 15 & 25 & 5 \\ 225 & -75 & -75 & -75 \end{bmatrix} \tag{56}$$

The derivatives ($\partial\varepsilon_{st}^{aux}/\partial\xi$, $\partial\varepsilon_{st}^{aux}/\partial\eta$), and $\partial\varepsilon_{st}^{aux}/\partial X_m$ ($m = 1,2$) can be obtained using Equations (53) and (54), respectively (same procedure as for the Q8 elements).

4.2.3. M-integral implementation for crack-tip elements. For the case in which crack-tip elements are included, the M-integral is recast as follows (cf. Equation (22)):

$$\begin{aligned} M_{local} = (M_1)_{local} = & \int_A \{\sigma_{ij}u_{i,1}^{aux} + \sigma_{ij}^{aux}u_{i,1} - \sigma_{ik}\varepsilon_{ik}^{aux}\delta_{1j}\}\frac{\partial q}{\partial x_j}\,dA \\ & + \int_A \left\{\underline{\sigma_{ij}(u_{i,1j}^{aux} - \varepsilon_{ij,1}^{aux})} - C_{ijkl,1}\varepsilon_{ij}\varepsilon_{kl}^{aux}\right\} q\,dA \end{aligned} \tag{57}$$

which is Equation (23) with $m = 1$. According to Section 3.2 (Equation (25)), the numerical implementation (FEM) of the M-integral is done in global co-ordinates ($m = 1,2$)

$$\begin{aligned} (M_m)_{global} = & \int_A \{\sigma_{ij}u_{i,m}^{aux} + \sigma_{ij}^{aux}u_{i,m} - \sigma_{ik}\varepsilon_{ik}^{aux}\delta_{mj}\}\frac{\partial q}{\partial X_j}\,dA \\ & + \int_A \{\underline{\sigma_{ij}(u_{i,mj}^{aux} - \varepsilon_{ij,m}^{aux})} - C_{ijkl,m}\varepsilon_{ij}\varepsilon_{kl}^{aux}\}q\,dA \end{aligned}$$

and then transformed to the local system according to Equation (26). In the above expression, the derivatives of the auxiliary strain field are obtained as follows:

$$\varepsilon^{\text{aux}}_{ij,m} = S_{ijkl,m}\sigma^{\text{aux}}_{kl} + S_{ijkl}\sigma^{\text{aux}}_{kl,m} \tag{58}$$

The approach given in Section 4.2.2 to compute $\varepsilon^{\text{aux}}_{ij,m}$ (see Equation (48)) for regular (non-singular) elements, (see Equation (53) for Q8 and T6) is not employed here because of the singular nature of the auxiliary strain field of $O(r^{-1/2})$ in the region with special crack-tip elements ($r \to 0$). An alternative and feasible approach consists of evaluating $C_{ijkl,m}$ (see expression above for $(M_m)_{\text{global}}$) and $S_{ijkl,m}$ (see Equation (58)) by using shape function derivatives, as shown below.

Let P denote the material property (either C_{ijkl} or S_{ijkl}). For crack-tip elements (T6qp), it is approximated as follows:

$$P(\xi,\eta) = b_1 + b_2\xi + b_3\eta + b_4\xi\eta \tag{59}$$

Using four Gauss points to sample the material property tensor components, one writes P as

$$P(\xi,\eta) = [1 \;\; \xi \;\; \eta \;\; \xi\eta]\;\mathbf{T}\;\mathbf{P}_G \tag{60}$$

where $\mathbf{P}_G$ denotes the material properties at the Gauss points. The derivatives ($\partial P/\partial\xi$, $\partial P/\partial\eta$), and $\partial P/\partial X_m$ ($m = 1, 2$) can be obtained by Equations (53) and (54), respectively.

5. NUMERICAL EXAMPLES

The performance of the M-integral method for extracting SIFs in FGMs is examined by means of numerical examples. In order to assess the various features of the method, the following examples are presented:

(1) Composite strip under mode I loading
(2) Plate with an interior inclined crack—direct versus indirect approaches
(3) Edge crack in an FGM strip
(4) Functionally graded coating with multiple parallel cracks
(5) Plate with a crack and a hole

All the examples are analysed using the FEM code I-FRANC2D[§] (Illinois–FRacture ANalysis Code 2D), which is based on the code FRANC2D [59, 60] developed at Cornell University. The I-FRANC2D code considers spatial changes in material properties (either by means of continuum functions or micromechanics models) and special techniques to evaluate mixed-mode SIFs in FGMs including the M-integral. The I-FRANC2D element library for FGMs consists of *graded elements* [23, 61, 62], which incorporate the material property gradient at the size-scale of the element. These elements are used either as regular elements, special crack tip elements or transition elements. The specific graded elements used here are based on the *generalized isoparametric formulation* presented by Kim and Paulino [23], who have also compared the performance of these elements with that of conventional homogeneous elements (produces a step-wise constant approximation to a continuous material property field) [62].

[§]The FEM code I-FRANC2D was formerly called FGM-FRANC2D [23].

All the examples are discretized with isoparametric graded elements using the I-FRANC2D code. In particular, singular quarter-point six-node triangles (T6qp) are used as crack-tip elements, eight-node serendipity elements (Q8) are used over most of the mesh, and T6 elements are used in the transition region between the T6qp and the Q8 elements. The mesh discretization of examples 1, 3, and 4 could be reduced further by means of symmetry, but was not due to meshing restrictions and to the fact that these meshes will be used for automatic crack propagation under general material variation, i.e. not necessarily in the directions used in this manuscript. Moreover, the discretization of these three examples allows one to check that the expected symmetries are present in the results of the analyses.

The first example uses the direct approach to evaluate derivatives of material properties (see Section 4), the second example compares both the direct and indirect (see Section 4 and Table I) approaches, and the remaining three examples use the indirect approach where material properties are obtained by means of micromechanics models with volume fraction distribution given by Equation (38) with $p = 1.0$. All the examples include SIF results. In addition, the first example addresses the convergence of the M-integral to evaluate SIFs as the region for the EDI becomes larger. The second example investigates the influence of the incompatibility in the M-integral formulation for FGMs. The third and last examples compare the influence of different micromechanics models (SCM, TPM, and MT) on Mode I and mixed-mode SIFs, respectively. The fourth example deals with periodic cracking in the graded coating layer of a coating/substrate system. The last example consists of a complicated geometry and boundary conditions for which there is no analytical or semi-analytical solution available and it represents a severe test of the FEM code and the M-integral implementation.

5.1. *Composite strip under mode I loading*

Figure 7(a) shows a composite strip with an edge crack of length a, Figure 7(b) illustrates the two types of material variation considered, Figure 7(c) shows the complete mesh configuration, and Figure 7(d) shows a mesh detail and contours using 8 sectors (S8) and 7 rings (R7) around the crack tip. The applied load corresponds to $\sigma_{22}(X_1, 1) = \bar{\varepsilon}\bar{E}(X_1) = \bar{\varepsilon}E(X_1)/(1-\nu^2)$, and this stress distribution was obtained by applying equivalent nodal forces along the top horizontal edge of the mesh. The displacement boundary condition is prescribed such that $u_2 = 0$ along the lower edge and $u_1 = 0$ for the node at the left hand side. This loading results in a uniform strain $\varepsilon_{22}(X_1, X_2) = \bar{\varepsilon}$ in a corresponding uncracked structure.

Young's modulus varies as a hyperbolic tangent function of X_1. Its expression and spatial derivative are given by

$$E(X_1) = \frac{E_1 + E_2}{2} + \frac{E_1 - E_2}{2} \tanh(\beta(X_1 + 0.1)) \tag{61}$$

$$\frac{\mathrm{d}E(X_1)}{\mathrm{d}X_1} = \frac{E_1 - E_2}{2} \beta[1 - \tanh^2(\beta(X_1 + 0.1))] \tag{62}$$

respectively, while Poisson's ratio is constant. Equations (61) and (62) are used in the direct approach (see Table I), which involves computation of the constitutive tensors $\mathbf{C}$ and $\mathbf{S}$

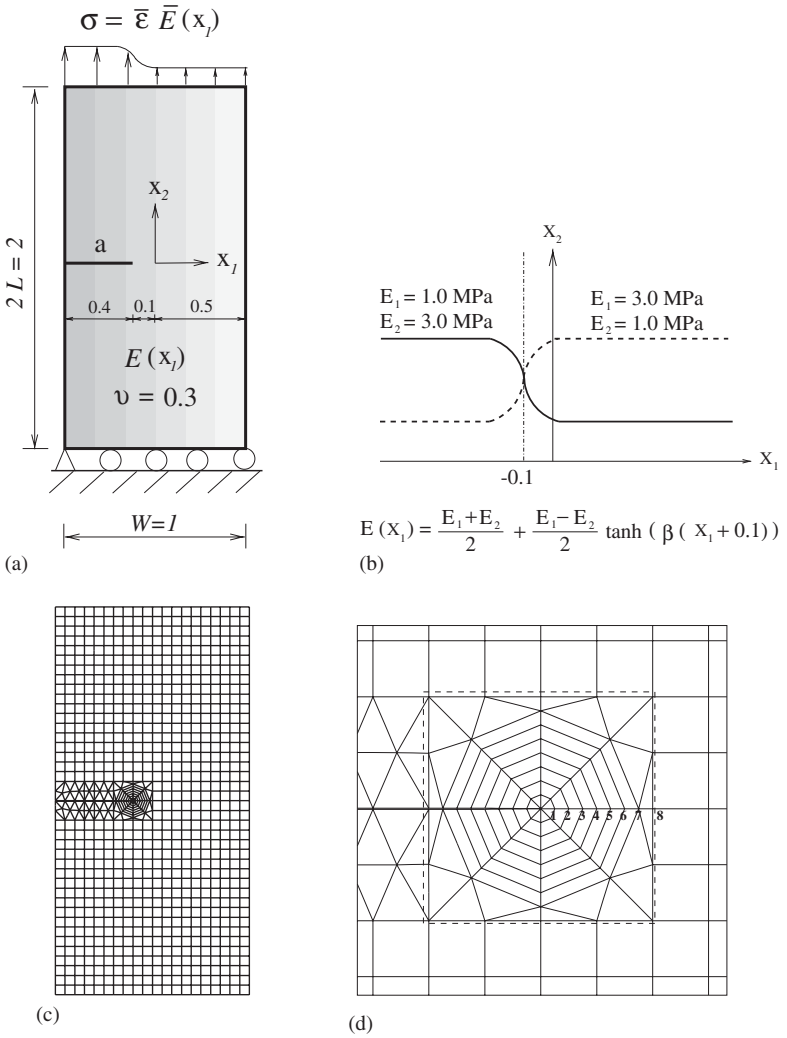

Figure 7. Example 1: composite strip: (a) geometry and BCs; (b) two types of material gradation; (c) typical finite element; and (d) mesh detail and 8 contours around the crack tip using 8 sectors (S8) and 7 rings (R7) of elements.

and their derivatives in the process of evaluating SIFs by means of the M-integral. Figure 8 shows the modulus variation in the interval $X_1 \in [-0.5, 0.5]$ considering $(E_1, E_2) = (1.0, 3.0)$ MPa for various values of the nonhomogeneity parameter βa. Notice that as $\beta a \to 20$ the material gradient becomes very steep. The mesh discretization consists of 807 Q8, 84 T6, and 8 T6qp elements, with a total of 899 elements and 2757 nodes. The following data were used

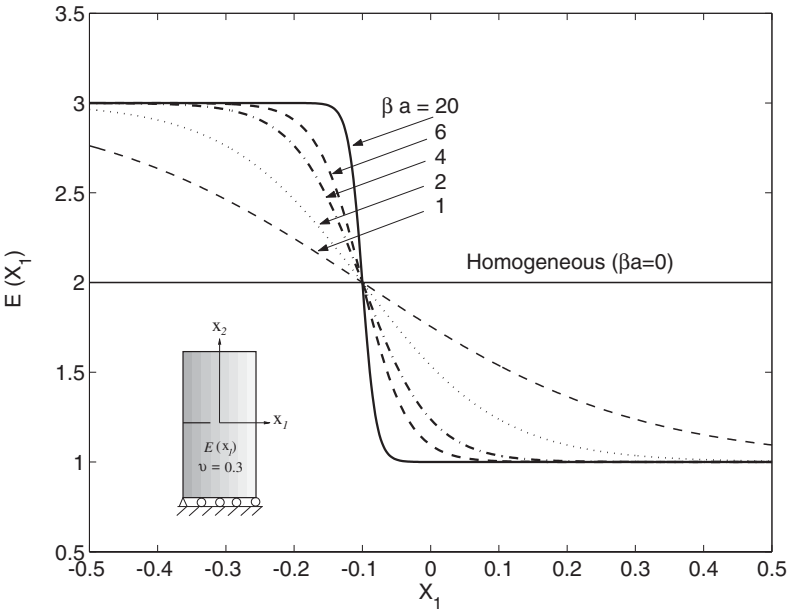

Figure 8. Example 1: material gradation profile considering $(E_1, E_2) = (1.0, 3.0)$MPa and various nonhomogeneity parameters βa.

Table II. Example 1: normalized SIFs $(K_{\mathrm{I}}/(\bar{\varepsilon}\bar{E}(-0.5)\sqrt{\pi a}))$ for a composite strip with $(E_1, E_2) = (1.0, 3.0)$ MPa.

		Rao and Rahman [10]		
β a	Direct	Method I	Method II	Eischen [22]
0	2.109	2.133	2.133	2.112
2	2.289	2.304	2.348	2.295
4	2.549	2.589	2.670	2.571
6	2.729	2.769	2.879	2.733
20	3.050	3.314	3.579	3.228

for the FEM analysis: $a/W = 0.4$; $L/W = 1.0$; $\beta a = 0, 2, 4, 6, 20$; $\bar{\varepsilon} = 1.0$; $v = 0.3$; plane strain; and 2×2 Gauss quadrature.

Tables II and III show normalized SIFs using the M-integral for two different material variations corresponding to $(E_1, E_2) = (1.0, 3.0)$MPa and $(E_1, E_2) = (3.0, 1.0)$MPa, respectively. Notice that the results for normalized SIFs agree well with reference solutions. Table II refers to the material variation illustrated by the solid line in Figure 7(b), and also by Figure 8. The present SIF results are in good agreement with the reference results of Eischen [22] using the J_k^*-integral method, and those of Rao and Rahman [10] using the element-free Galerkin method and two techniques to evaluate the M-integral (Method I uses a constant constitutive tensor at the crack tip region and Method II uses a spatially varying constitutive tensor).

Table III. Example 1: normalized SIFs $(K_I/(\bar{\varepsilon}\bar{E}(+0.5)\sqrt{\pi a}))$ for a composite strip with $(E_1, E_2) = (3.0, 1.0)$ MPa.

β a	Direct	MCC
0	2.109	2.099
2	0.856	0.858
4	0.732	0.740
6	0.684	0.696
20	0.584	0.620

Table IV. Example 1: convergence of normalized SIFs $(K_I/(\bar{\varepsilon}\bar{E}(-0.5)\sqrt{\pi a}))$ for a composite strip with $(E_1, E_2) = (1.0, 3.0)$ MPa and $\beta a = 4.0$ (see Figure 7(d)).

Contour	SIF
1	2.565
2	2.544
3	2.546
4	2.548
5	2.548
6	2.549
7	2.549
8	2.549

Table III refers to the material variation illustrated by the dashed line of Figure 7(b). The SIF results are in good agreement with those obtained by the modified crack closure (MCC) method presented by Kim and Paulino [23]. Because the results are normalized, it is worth mentioning that the magnitude of SIFs for FGMs in Table III are actually lower than the corresponding ones in Table II. In both Tables II and III, the biggest discrepancy in the comparative results occurs for $\beta a = 20$. This is expected because this case corresponds to the steepest material gradation (see Figure 8).

Table IV shows convergence of normalized SIFs for $\beta a = 4.0$ considering 8 contours as shown in Figure 7(d). Each contour is a ring of elements completely surrounding the crack tip from one crack face to the opposite crack face. The SIFs are obtained by means of the equivalent domain integral (EDI) implementation and they converge quickly to the final result.

5.2. Plate with an interior inclined crack—direct versus indirect approaches

Konda and Erdogan [63] have investigated the mixed-mode crack problem in an unbounded nonhomogeneous elastic medium considering plane state conditions (either generalized plane stress or plane strain). The crack is arbitrarily oriented with respect to the material property gradient. This problem is solved here by means of the FEM by considering a plate that is large relative to the crack size $(a/W = 0.1)$, as illustrated by Figure 9(a), which shows an interior inclined crack of length $2a$ with angle θ in a finite two-dimensional plate, Figure 9(b)

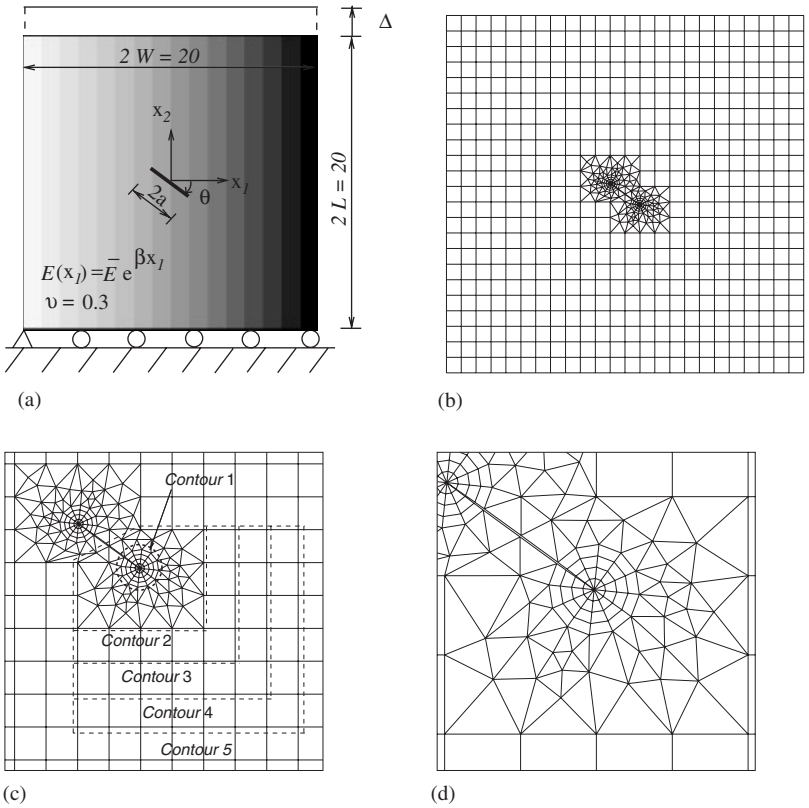

Figure 9. Example 2: FGM plate with an inclined crack with angle θ: (a) geometry and BCs under fixed-grip loading; (b) typical finite element mesh; (c) contours for EDI computation of M-integral; (d) mesh detail using 12 sectors (S12) and 4 rings (R4) around the crack tips ($\theta = 36^\circ$ clockwise).

shows a typical mesh configuration, Figure 9(c) shows the five contours used to evaluate the M-integral, and Figure 9(d) shows a mesh detail using 12 sectors (S12) and four rings (R4) around the crack tip. The applied load corresponds to $\sigma_{22}(X_1, 10) = \bar{\varepsilon}\bar{E}e^{\beta X_1}$, and this stress distribution was obtained by applying equivalent nodal forces along the top horizontal edge of the mesh. The displacement boundary condition is prescribed such that $u_2 = 0$ along the lower edge and $u_1 = 0$ for the node at the left hand side. This loading results in a uniform strain $\varepsilon_{22}(X_1, X_2) = \bar{\varepsilon}$ in a corresponding uncracked structure.

Young's modulus is an exponential function of X_1, while Poisson's ratio is constant ($\nu = 0.3$). The typical mesh discretization consists of 1565 Q8, 173 T6, and 24 T6qp elements, with a total of 1762 elements and 5344 nodes. The following data were used for the FEM analysis: $a/W = 0.1$; $L/W = 1.0$; $E(X_1) = \bar{E}e^{\beta X_1}$; $\bar{E} = 1.0$; $\theta/\pi = (0.0 \text{ to } 1.0)$; $\beta a = 0.0, 0.5$; $\bar{\varepsilon} = 1.0$; $\nu = 0.3$; plane stress; and 2×2 Gauss quadrature.

Figure 10 shows the normalized SIFs at the right crack tip as a function of the crack inclination angle θ computed by using the direct approach of the M-integral for both $\beta a = 0$ (homogeneous material) and $\beta a = 0.5$ (FGM). Figure 11 shows an analogous plot for the left

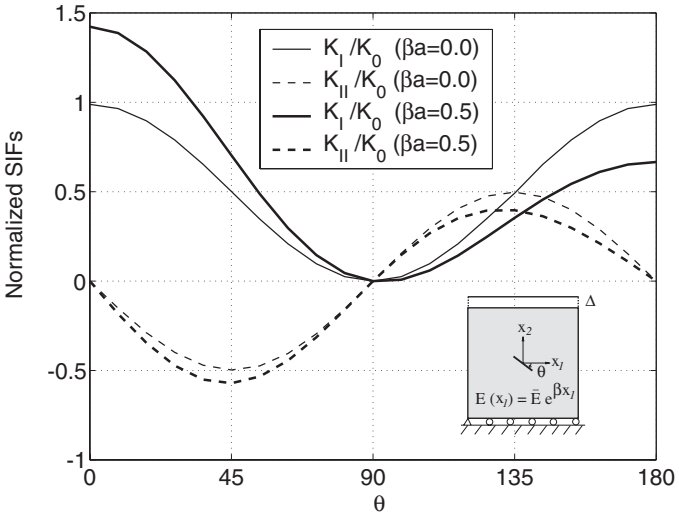

Figure 10. Example 2: normalized SIFs versus angle θ (measured clockwise) for the *right* crack tip of an interior inclined crack in a plate ($K_0 = \bar{\varepsilon}\bar{E}\sqrt{\pi a}$).

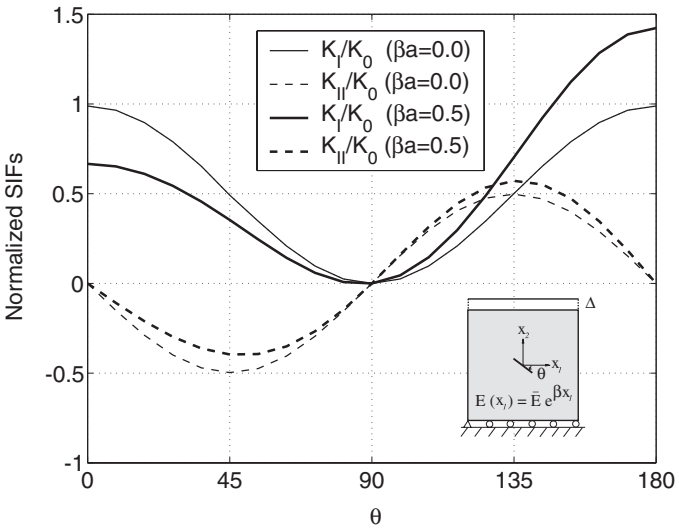

Figure 11. Example 2: normalized SIFs versus angle θ (measured clockwise) for the *left* crack tip of an interior inclined crack in a plate ($K_0 = \bar{\varepsilon}\bar{E}\sqrt{\pi a}$).

crack tip. A comparison between Figures 10 and 11 reveals that for homogeneous materials ($\beta a = 0$) the SIFs at the left and right crack tips are approximately the same because the plate is large relative to the crack length ($a/W = a/L = 0.1$). By the symmetry of the FGM problem illustrated in Figure 9, the SIFs at the left and right crack tips are related as follows:

Table V. Example 2: comparison of normalized mixed-mode SIFs for the direct approach ((S12, R4) and $K_0 = \bar{\varepsilon}\bar{E}\sqrt{\pi a}$). The FGM is characterized by the nonhomogeneity parameter $\beta a = 0.5$ (see Figure 9).

Method	θ°	K_{I}^{+}/K_0	K_{II}^{+}/K_0	K_{I}^{-}/K_0	K_{II}^{-}/K_0
Konda and Erdogan [63]	0	1.424	0.000	0.674	0.000
	18	1.285	−0.344	0.617	−0.213
	36	0.925	−0.548	0.460	−0.365
	54	0.490	−0.532	0.247	−0.397
	72	0.146	−0.314	0.059	−0.269
	90	0.000	0.000	0.000	0.000
Present	0	1.4234	0.0000	0.6657	0.0000
	18	1.2835	−0.3461	0.6104	−0.2109
	36	0.9224	−0.5510	0.4559	−0.3621
	54	0.4881	−0.5344	0.2451	−0.3940
	72	0.1451	−0.3147	0.0587	−0.2670
	90	0.0000	0.0000	0.0000	0.0000
Dolbow and Gosz [9] (X-FEM)	0	1.445	0.000	0.681	0.000
	18	1.303	−0.353	0.623	−0.213
	36	0.930	−0.560	0.467	−0.364
	54	0.488	−0.540	0.251	−0.396
	72	0.142	−0.316	0.062	−0.268
	90	0.000	0.000	0.000	0.000

$K_{\mathrm{I}}^{\mathrm{L}}(\theta) = K_{\mathrm{I}}^{\mathrm{R}}(\pi - \theta)$ and $K_{\mathrm{II}}^{\mathrm{L}}(\theta) = -K_{\mathrm{II}}^{\mathrm{R}}(\pi - \theta)$. This trend is observed in the numerical results of Figures 10 and 11. Table V compares the normalized mixed-mode SIFs obtained by the direct approach (using 12 sectors (S12) and 4 rings (R4) of elements around the crack tips) considering $\beta a = 0.5$ with the reference results by Konda and Erdogan [63] and the numerical results by Dolbow and Gosz [9], who used 60×60 quadrilateral elements for the X-FEM mesh discretization. The error in our calculations ranges from 0 to 1.3%, and the overall average error is 0.64%. Moreover, our numerical values on average appear to be more accurate than those reported by Dolbow and Gosz [9], which may be due to the careful crack-tip discretization used in the present investigation.

Figures 12 and 13 compare normalized SIFs computed by both including and neglecting the incompatibility terms (see Equation (25)) in the M-integral formulation. Notice that the converged solution is obtained when including the incompatibility term, however, such behaviour is not observed when neglecting the incompatibility term. Analogous observations have also been made by Dolbow and Gosz [9] using the extended finite element method (X-FEM).

In order to assess the accuracy of the indirect approach in comparison with the direct approach, the M-integral is evaluated by both approaches for the problem described above (see Figure 9). To this end, the indirect approach is employed considering the same material properties used for the direct approach, i.e. $E(X_1) = \bar{E}\mathrm{e}^{\beta X_1}$, $\nu = 0.3$; however, the analytical expression for the modulus is not used to obtain closed form expressions for the derivatives of material properties. Instead, the numerical evaluation of derivatives is employed (see Section 4.2.3). Therefore, it is expected that the normalized SIF results for the indirect

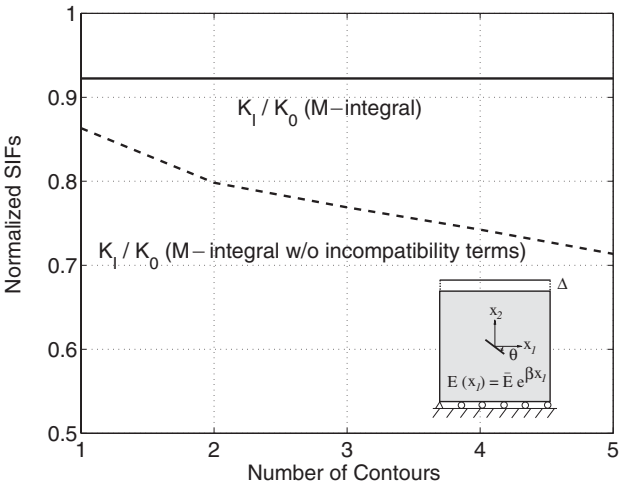

Figure 12. Example 2: comparison of normalized SIFs (K_{I}) using M-integral both considering and neglecting incompatibility terms for the right crack tip of an inclined crack with angle $\theta = 36^\circ$ clockwise ($K_0 = \bar{\varepsilon}\bar{E}\sqrt{\pi a}$).

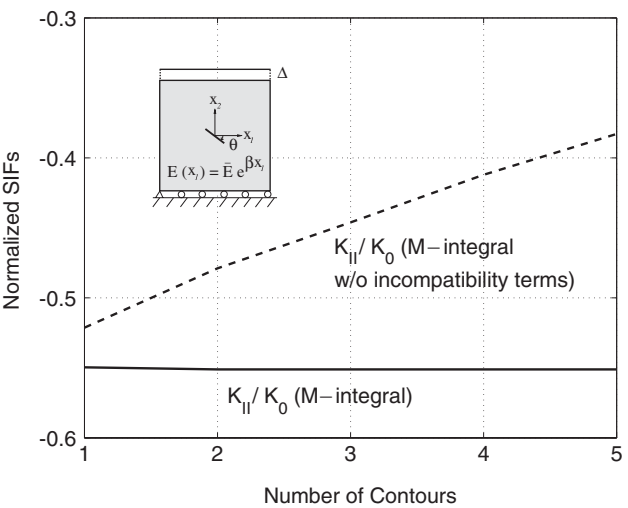

Figure 13. Example 2: comparison of normalized SIFs (K_{II}) using M-integral both considering and neglecting incompatibility terms for the right crack tip of an inclined crack with an angle $\theta = 36^\circ$ clockwise ($K_0 = \bar{\varepsilon}\bar{E}\sqrt{\pi a}$).

approach are not as accurate as those for the direct approach. This statement can be verified by examining the data given in Table VI, which shows a comparison of normalized mixed-mode SIFs computed with 12 sectors (S12) and 4 rings (R4) of elements around the crack tips and considering the length scale of nonhomogeneity $\beta a = 0.5$. Notice that the

Table VI. Example 2: comparison of normalized mixed-mode SIFs for the direct and indirect approaches ($K_0 = \bar{\varepsilon}\bar{E}\sqrt{\pi a}$). The FGM is characterized by the nonhomogeneity parameter $\beta a = 0.5$ (see Figure 9).

Method	θ°	K_{I}^{+}/K_0	K_{II}^{+}/K_0	K_{I}^{-}/K_0	K_{II}^{-}/K_0
Konda and	18	1.285	−0.344	0.617	−0.213
Erdogan [63]	36	0.925	−0.548	0.460	−0.365
	72	0.146	−0.314	0.059	−0.269
Direct	18	1.2835	−0.3461	0.6104	−0.2109
(S12,R4)	36	0.9224	−0.5510	0.4559	−0.3621
	72	0.1451	−0.3147	0.0578	−0.2670
Indirect	18	1.2970	−0.3373	0.6053	−0.2082
(S12,R4)	36	0.9230	−0.5390	0.4559	−0.3551
	72	0.1446	−0.3184	0.0534	−0.2659

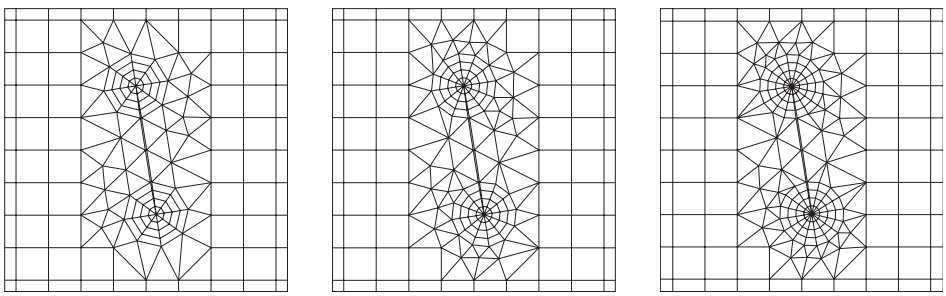

(a) S8, R4 (b) S12, R4 (c) S16, R4

Figure 14. Example 2: mesh detail using 4 rings (R4) of elements and various sectors around the crack tips and $\theta = 81^\circ$: (a) 8 sectors (S8); (b) 12 sectors (S12); and (c) 16 sectors (S16).

normalized SIF results for the direct approach are in remarkable agreement with those by Konda and Erdogan [63] (maximum difference 2.1%, average difference 0.71%), however, (as expected) the results by the indirect approach (maximum difference 9.5%, average difference 2.16%) are worse, especially as the angle θ (defining the crack inclination) increases.

To achieve a level of accuracy comparable to that of the direct approach, the indirect approach can be improved by means of a local selective mesh refinement around the crack tip, which can be done either with respect to the hoop (number of sectors) or the radial (number of rings) discretizations. The former point is illustrated by Figure 14 and Table VII, and the latter point is discussed in the next paragraph. Figure 14 shows three mesh details using a fixed number of rings (R4) and a variable number of sectors (S8, S12, S16) considering $\theta = 81^\circ$ (crack inclination angle) for the FGM plate of Figure 9(a). Table VII shows the reference normalized SIFs given by Dong and Paulino [64] in addition to those obtained by the direct (S12) and indirect (S8, S12, S16) approaches. Such reference results for $\theta = 81^\circ$ are not available from Konda and Erdogan [63]. Table VII indicates that the normalized SIF results obtained with the indirect approach are quite sensitive to the crack tip discretization, especially K_{I}^{-}/K_0. To obtain results comparable to the S12 discretization by the direct approach, at least an S16 discretization is needed by the indirect approach.

Table VII. Example 2. normalized mixed-mode SIFs at the tips of a crack inclined at angle $\theta = 81^\circ$: direct versus indirect approaches ((R4) and $K_0 = \bar{\varepsilon}\bar{E}\sqrt{\pi a}$). The FGM is characterized by the nonhomogeneity parameter $\beta a = 0.5$ (see Figure 14).

Method	Sectors	K_I^+/K_0	K_{II}^+/K_0	K_I^-/K_0	K_{II}^-/K_0
Dong and Paulino [64]	—	0.0452	−0.1595	0.0072	−0.1473
Direct	S12	0.0448	−0.1608	0.0073	−0.1464
	S8	0.0420	−0.1625	0.0031	−0.1422
Indirect	S12	0.0392	−0.1638	0.0050	−0.1446
	S16	0.0470	−0.1624	0.0065	−0.1462

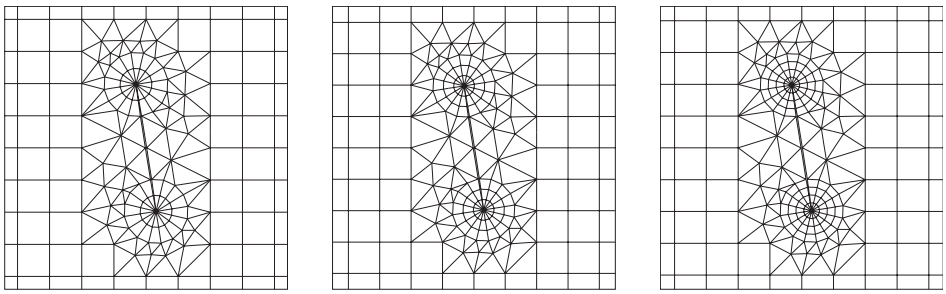

(a) S16, R2 (b) S16, R3 (c) S16, R4

Figure 15. Example 2: mesh detail using 16 sectors (S16) and various rings of elements around the crack tips and $\theta = 81^\circ$: (a) 2 rings (R2); (b) 3 rings (R3); (c) 4 rings (R4).

Table VIII. Example 2: normalized mixed-mode SIFs at the crack tips of a crack at angle $\theta = 81^\circ$ using indirect approaches: including versus excluding first ring of crack-tip elements ((S16) and $K_0 = \bar{\varepsilon}\bar{E}\sqrt{\pi a}$). The FGM is characterized by the nonhomogeneity parameter $\beta a = 0.5$ (see Figure 15).

Method		Rings	K_I^+/K_0	K_{II}^+/K_0	K_I^-/K_0	K_{II}^-/K_0
Dong and Paulino [64]		—	0.0452	−0.1595	0.0072	−0.1473
Indirect	Included	R2	0.0477	−0.1625	0.0064	−0.1461
		R3	0.0472	−0.1624	0.0062	−0.1462
		R4	0.0470	−0.1624	0.0065	−0.1462
	Excluded	R2	0.0475	−0.1675	0.0058	−0.1417
		R3	0.0470	−0.1654	0.0058	−0.1442
		R4	0.0469	−0.1642	0.0063	−0.1448

Figure 15 shows three mesh details using a fixed number of sectors (S16) and a variable number of rings (R2, R3, R4) considering $\theta = 81^\circ$ (crack inclination angle) for the FGM plate of Figure 9(a). Table VIII shows the reference normalized SIFs given by Dong and Paulino [64] in addition to those obtained by the indirect approach both including and excluding the crack-tip elements. As stated above, such reference results for $\theta = 81^\circ$ are not available from

Table IX. Example 2: comparison of normalized SIFs either including or excluding crack-tip elements around the crack tip (S16, R4) using indirect approaches ($K_0 = \bar{\varepsilon}\bar{E}\sqrt{\pi a}$). The FGM is characterized by the nonhomogeneity parameter $\beta a = 0.5$.

Method		θ°	K_I^+/K_0	K_{II}^+/K_0	K_I^-/K_0	K_{II}^-/K_0
Reference values [63, 64]		0	1.424	0	0.674	0
		18	1.285	−0.344	0.617	−0.213
		36	0.925	−0.548	0.460	−0.365
		54	0.490	−0.532	0.247	−0.397
		72	0.146	−0.314	0.059	−0.269
		81	0.0452	−0.1595	0.0072	−0.1473
		90	0	0	0	0
Indirect	Included	0	1.4262	0	0.6612	0
		18	1.2835	−0.3350	0.6076	−0.2121
		36	0.9156	−0.5280	0.4489	−0.3587
		54	0.4876	−0.5239	0.2414	−0.3920
		72	0.1486	−0.3145	0.0550	−0.2655
		81	0.0470	−0.1624	0.0065	−0.1462
		90	0	0	0	0
	Excluded	0	1.4415	0	0.6550	0
		18	1.2953	−0.3420	0.6019	−0.2085
		36	0.9218	−0.5372	0.4463	−0.3536
		54	0.4893	−0.5309	0.2406	−0.3873
		72	0.1488	−0.3179	0.0550	−0.2630
		81	0.0469	−0.1642	0.0063	−0.1448
		90	0	0	0	0

Konda and Erdogan [63]. Table VIII indicates that four rings of elements (R4) best estimate the normalized SIFs for both cases, i.e. 'including' and 'excluding' the first ring of crack-tip elements.

Based on the above results, the best combination of mesh refinement for the indirect approach consists of 16 sectors (S16) and 4 rings (R4) of elements. This combination is used for evaluating the normalized SIFs shown in Table IX. Table IX shows the FEM results for normalized SIFs using the indirect approach by considering and neglecting crack-tip elements in comparison with those reference results by Konda and Erdogan [63] and Dong and Paulino [64]. The case 'including' crack-tip elements produces on average higher accuracy of SIFs (maximum difference 9.8%, average difference 2.28%) than the case 'excluding' crack-tip elements (maximum difference 12.5%, average difference 2.55%)—the maximum difference occurs for $\theta = 81^\circ$. Thus for the remaining three examples using the indirect approach, the crack-tip elements are included in all the calculations.

5.3. Edge crack in an FGM strip

Figure 16(a) shows a long FGM strip with an edge crack of length 'a', Figures 16(b) and 16(c) illustrate the tension and bending loadings, respectively, applied on the top and bottom edges, Figure 16(d) shows the typical finite element mesh discretization, and Figure 16(e) shows the crack tip mesh detail using 16 sectors (S16) and 4 rings (R4) of

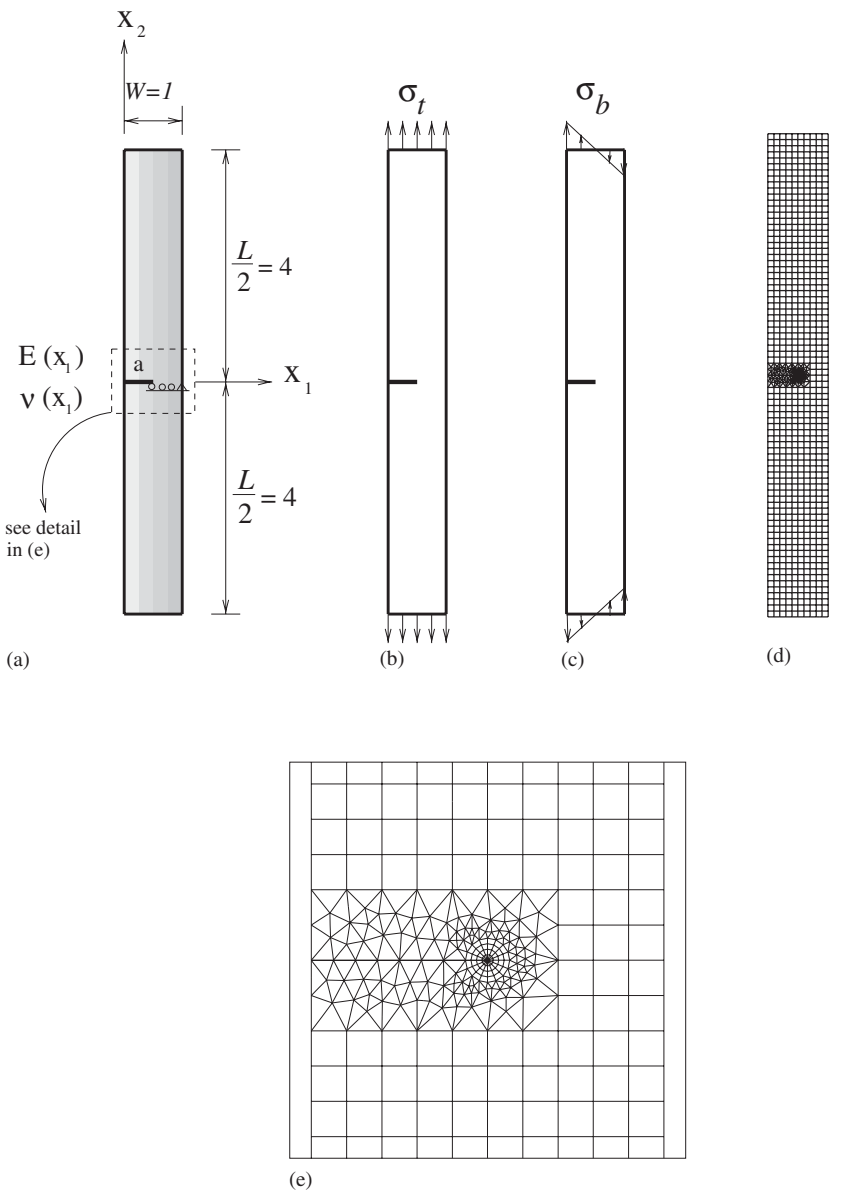

Figure 16. Example 3: FGM plate: (a) geometry, BCs, and material properties; (b) tension loading; (c) bending loading; (d) typical finite element mesh; and (e) mesh detail using 16 sectors (S16) and 4 rings (R4) around the crack tip.

elements. The applied load corresponds to $\sigma_{22}(X_1, \pm 4) = \pm 1$ for tension and $\sigma_{22}(X_1, \pm 4) = \pm (-2X_1 + 1)$ for bending. The displacement boundary condition is prescribed such that $u_2 = 0$ on the crack tip node and $u_1 = u_2 = 0$ for the node in the middle of the right edge.

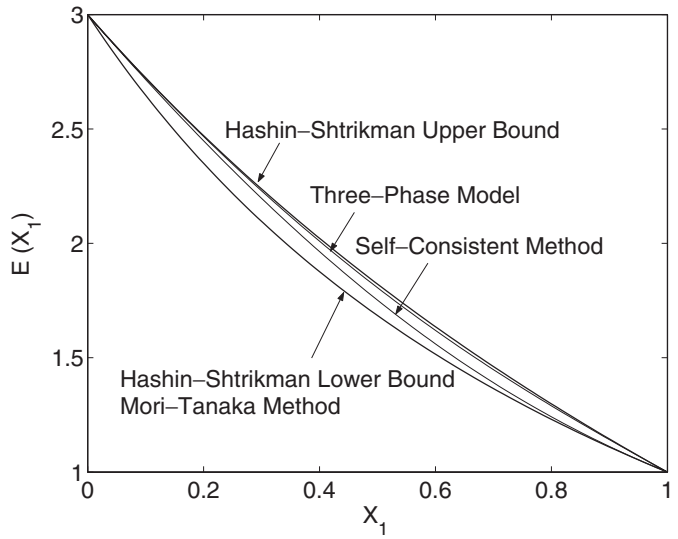

Figure 17. Examples 3 and 4: variation of Young's modulus for various micromechanics models.

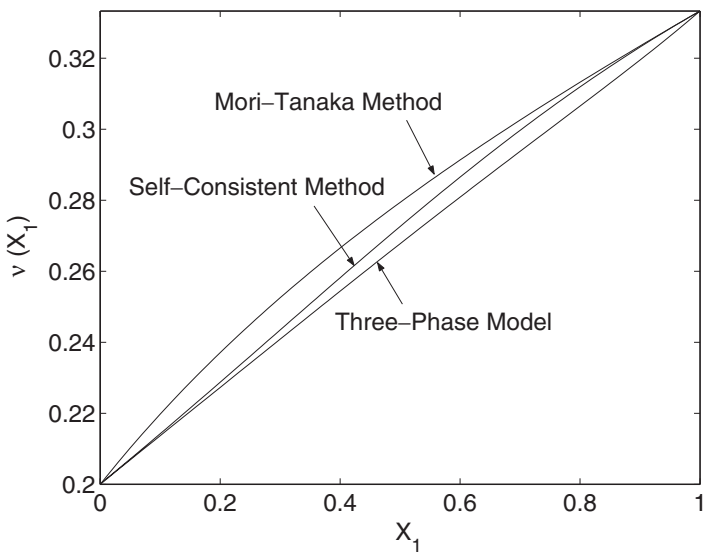

Figure 18. Examples 3 and 4: variation of Poisson's ratio for various micromechanics models.

The effective material properties for Young's modulus (E) and Poisson's ratio (ν) are obtained using the self-consistent (SCM), the three-phase (TPM), and the Mori–Tanaka (MT) methods. Figures 17 and 18 show the variation of Young's modulus and Poisson's ratio using each of these models. The mesh discretization consists of 821 Q8, 230 T6, and 16 T6qp elements, with a total of 1067 elements and 3159 nodes. The following data were used for the FEM analysis: $a/W = 0.25, 0.5, 0.75$; $L/W = 8$; $E_1 = 3$; $\nu_1 = 0.2$; $E_2 = 1$; $\nu_2 = 0.3333$; plane stress; and 2×2 Gauss quadrature.

Table X. Example 3: SIFs for an edge crack in a long FGM strip under tension and bending loads.

		Tension			Bending		
Method	a	SCM	TPM	MT	SCM	TPM	MT
	0.25	1.391	1.392	1.398	1.235	1.225	1.225
M-integral	0.50	3.935	3.914	3.905	2.222	2.207	2.198
	0.75	13.90	13.89	13.87	5.762	5.751	5.744
	0.25	1.408	1.408	1.414	1.248	1.238	1.237
MCC	0.50	3.933	3.915	3.907	2.224	2.210	2.201
	0.75	13.62	13.83	13.58	5.588	5.579	5.571

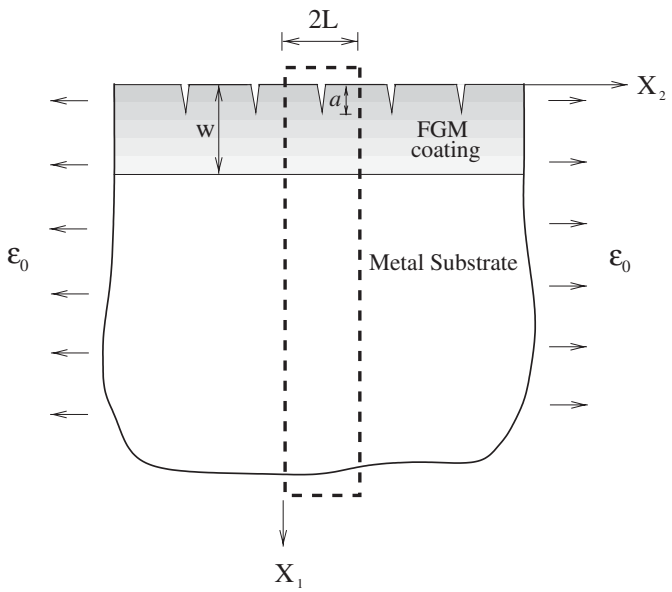

Figure 19. Example 4: periodic multiple cracks in an FGM coating/substrate system.

Table X shows FEM results for SIFs using the *M*-integral in comparison with those of the modified crack closure method (MCC) [65] for both tension and bending loadings. The present SIF results agree well with the MCC. Notice that, for both loading cases, the SIFs increase as the crack length *a* increases, and the SIFs obtained by using SCM, TPM and MT are similar because the material variation profile provided by these three models are also similar. For instance, notice the narrow range of Young's modulus and Poisson's ratio variations shown in Figures 17 and 18, respectively.

5.4. Functionally graded coating with multiple parallel cracks

This example, which is illustrated by Figure 19, was studied by Bao and Wang [28]. Figure 20(a) shows a typical unit of periodic multiple cracks of length *a* located in a

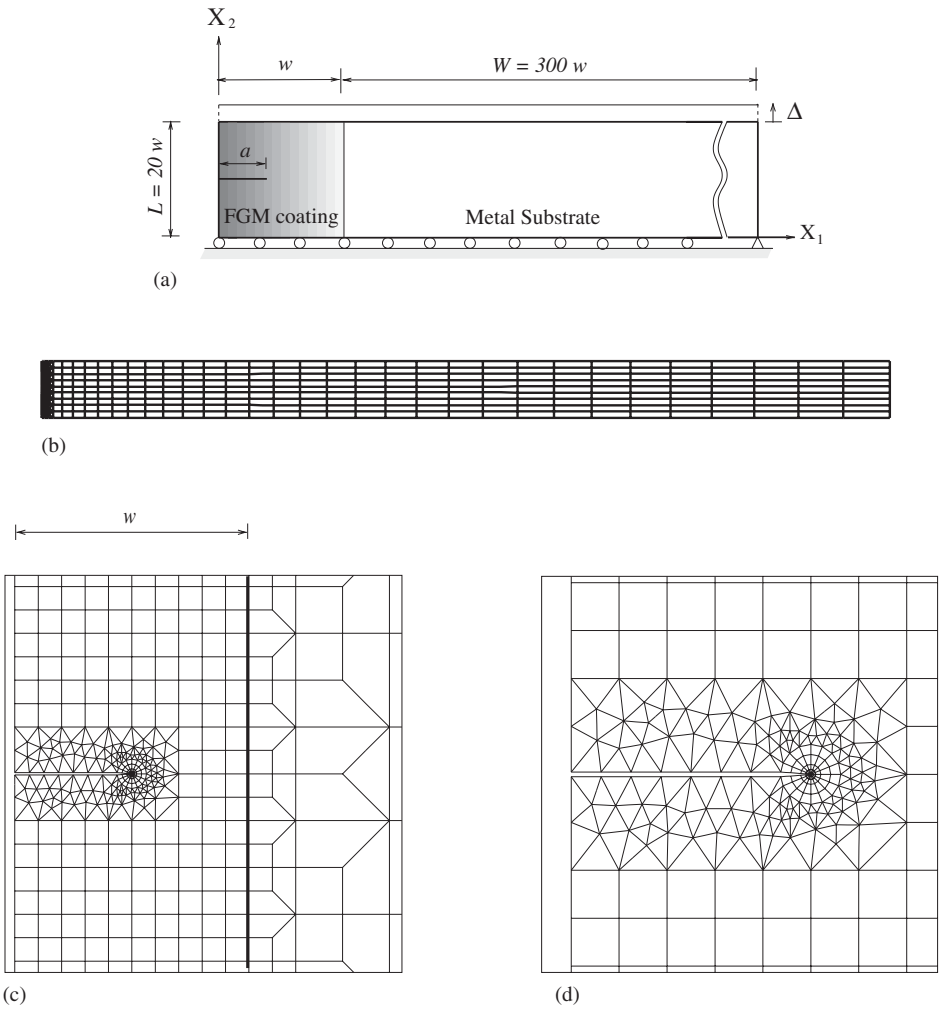

Figure 20. Example 4: typical unit of multiple cracks in coating/substrate system under constant displacement loading: (a) geometry and BCs; (b) complete finite element mesh; (c) mesh detail along the graded coating region; and (d) zoom around the crack tip using 16 sectors (S16) and 4 rings (R4) of elements.

coating/substrate system under fixed grip loading, Figure 20(b) shows the complete finite mesh configuration, Figure 20(c) shows a detail around the coating graded region, and Figure 20(d) shows a zoom around the crack tip using 16 sectors (S16) and 4 rings (R4) of elements.

The applied displacements correspond to $u_2(0 \leqslant X_1 \leqslant 301, 20) = \Delta = 1.0$ along the top edge. The displacement boundary condition is prescribed such that $u_1 = u_2 = 0$ for the corner node on the right and bottom edges and $u_2 = 0$ for the nodes of the bottom edge—see Figure 20(a).

The effective material properties for Young's modulus (E) and Poisson's ratio (v) are obtained using the three-phase model (TPM). Figures 17 and 18 show the variation of Young's

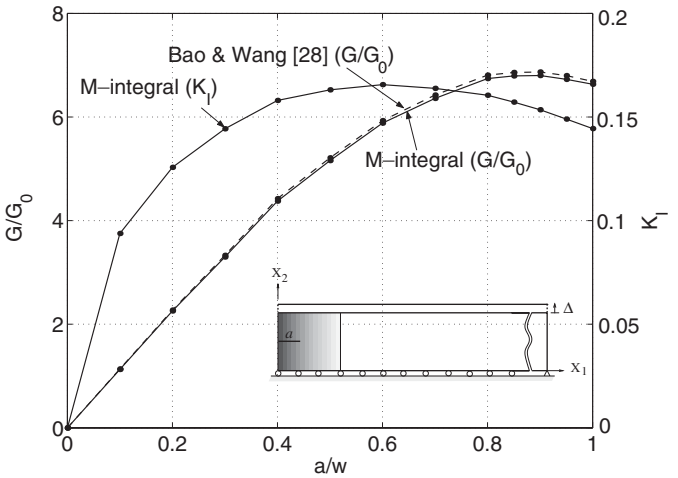

Figure 21. Example 4: normalized energy release rates (left axis) and mode I SIF K_{I} (right axis) versus crack length. For this example, $G_0 = \sigma^2 w/E'_m$ and $E'_m = E_m/(1-\nu_m^2)$.

modulus and Poisson's ratio for the graded region. The mesh discretization consists of 881 Q8, 225 T6, and 16 T6qp elements, with a total of 1122 elements and 3246 nodes. The following data were used for the FEM analysis: $a/w = 0.0$ to 1.0; $L = 20; w = 1; W = 300$; $E_1 = 3$; $\nu_1 = 0.2$; $E_2 = 1$; $\nu_2 = 0.3333$; plane strain; and 2×2 Gauss quadrature. Figure 21 shows normalized energy release rates and mode I SIF (K_{I}) versus the crack length a/w. The energy release rate is evaluated using $\mathcal{G} = K_{\mathrm{I}}^2/E'_{\mathrm{tip}}$, and the results are normalized with respect to $\mathcal{G}_0 = \sigma^2 w/E'_m$ where $E'_m = E_m/(1-\nu_m^2)$. The average stress σ corresponding to the applied strain $\varepsilon^0 = \Delta/L$ is obtained as [28]

$$\sigma = \frac{\varepsilon^0}{w+W}\left[W\frac{E_m}{1-\nu_m^2} + \int_0^w \frac{E(X_1)}{1-\nu^2(X_1)}\,\mathrm{d}x\right] \tag{63}$$

which is used to obtain $\mathcal{G}_0$. Figure 21 shows an excellent agreement of normalized energy release rates between our results and those by Bao and Wang [28]. Notice also that the mode I SIF (K_{I}) increases as the normalized crack length varies from 0 to 0.6, but decreases as it goes from 0.6 to 1.0. The trends for $\mathcal{G}$ and K differ, as well as the locations for their peak values.

5.5. *Plate with a crack and a hole*

The motivation for this example is to validate the numerical procedure of the interaction integral method in various aspects such as micromechanics models, an inclined material gradation, a crack interacting with a hole, and a complicated geometry. This example also shows capabilities and advantages of the present FEM implementation for general problems.

Figure 22(a) shows an FGM plate of complicated geometry with a crack of length a emanating from a hole. The material properties change along a line inclined at 30° with the Cartesian axes, which illustrates the case of a general material gradation. The material properties considered here are those of a SiC/C (silicon-carbide/carbon) FGM system [54]. Figures 22(b)

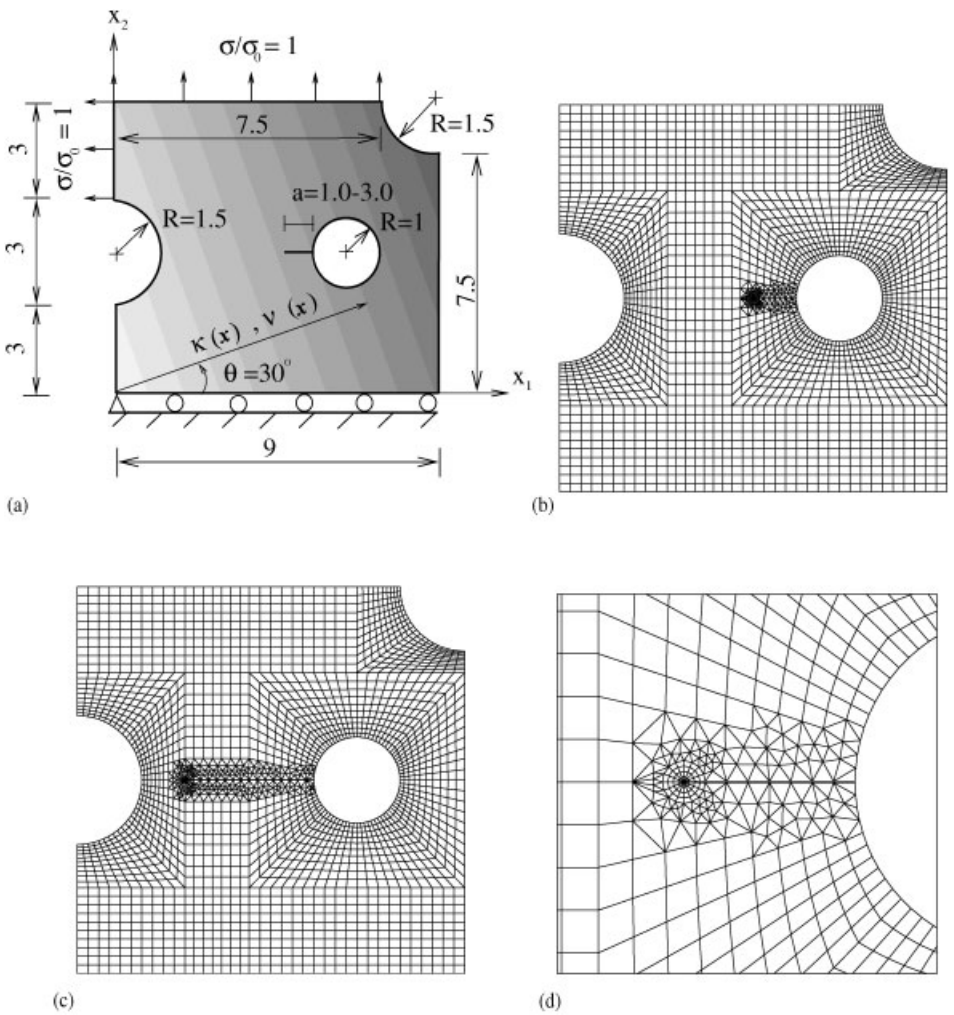

Figure 22. Example 5: FGM plate with a crack emanating from a hole: (a) geometry and BCs (units: GPa, mm); (b) finite element mesh for $a = 1.0$; (c) finite element mesh for $a = 3.0$; (d) mesh detail showing 16 sectors (S16) and 4 rings (R4) of elements around the crack tip for the case $a = 1.0$.

and 22(c) show the complete finite element meshes for $a = 1.0$ and 3.0, respectively, and Figure 22(d) shows the mesh detail around the crack tip for $a = 1.0$.

The applied load corresponds to $\sigma_{22}(X_1, 9)/\sigma_0 = 1$ GPa and $\sigma_{11}(0, 6 \leqslant X_2 \leqslant 9)/\sigma_0 = -1$ GPa, where σ_0 is a reference quantity that scales the applied stress. The displacement boundary condition is prescribed such that $u_2 = 0$ along the lower edge and $u_1 = 0$ for the node at the left hand side.

The effective material properties for bulk modulus (κ) and Poisson's ratio (ν) are obtained using the self-consistent (SCM), three phase (TPM), and Mori–Tanaka (MT) methods. Figures 23 and 24 show the variation of bulk modulus and Poisson's ratio. Notice that the

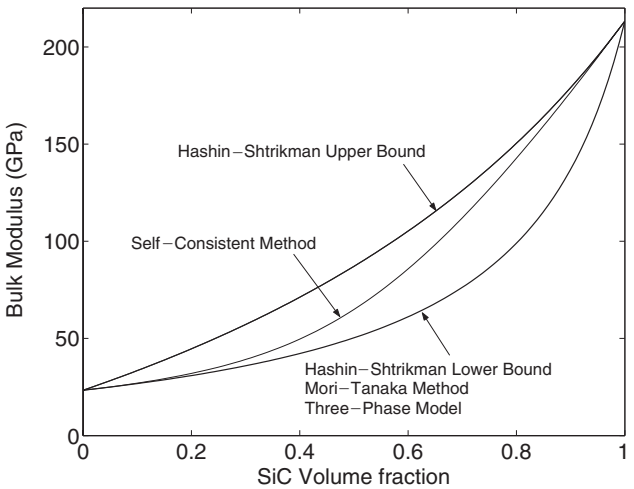

Figure 23. Example 5: variation of bulk modulus for micromechanics models.

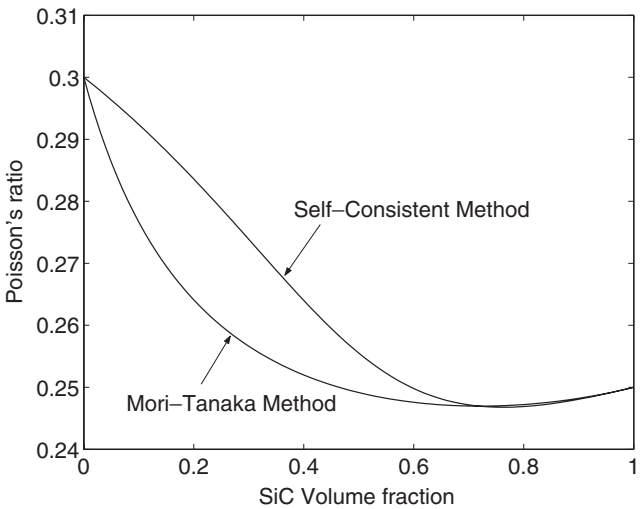

Figure 24. Example 5: variation of Poisson's ratio for micromechanics models.

range of material property variation is wider than in Example 3 (cf. Figures 24 and 18). This wide range of properties significantly influences the results obtained by using each micromechanics model. The typical mesh discretization consists of 2130 Q8, 204 T6, and 16 T6qp with a total of 2350 elements and 7190 nodes. The following data were used for the FEM analysis: $a/W = 1.0$ to 3.0; $L/W = 1.0$; $E_C = 28$ GPa; $v_c = 0.3$; $E_{\mathrm{SiC}} = 320$ GPa; $v_{\mathrm{SiC}} = 0.25$; plane stress; and 2×2 Gauss quadrature. The basic two-phase material properties were obtained from Zuiker's paper [54].

Table XI. Example 5: SIFs for an FGM plate with a crack emanating from a hole.

	SCM		TPM		MT	
a	K_{I}	K_{II}	K_{I}	K_{II}	K_{I}	K_{II}
1.0	2.316	−1.508	2.403	−1.467	2.248	−1.427
1.5	2.459	−1.740	2.570	−1.729	2.418	−1.675
2.0	2.642	−1.890	2.755	−1.921	2.625	−1.853
2.5	2.954	−2.003	3.098	−2.087	2.957	−2.002
3.0	3.548	−2.138	3.687	−2.292	3.569	−2.207

Table XI shows FEM results for SIFs using the M-integral for different crack lengths. As expected, the SIFs increase as the crack length a increases. Moreover, the SIF results obtained from the SCM, TPM, and MT differ more from one another than in Example 3 (cf. Tables X and XI) due to the wider range of material property variation (cf. Figures 24 and 18).

6. CONCLUDING REMARKS AND EXTENSIONS

This paper presents an accurate and robust scheme for evaluating mixed-mode SIFs by means of the interaction integral (M-integral) method considering arbitrarily oriented cracks in two-dimensional (2D) elastic FGMs. The scheme is robust in the sense that reasonable SIF estimates can be obtained with relatively coarse meshes. Two kinds of numerical implementations have been developed: direct approach for continuum models and indirect approach for micromechanics models. The latter is a generalized scheme which can handle any type of material gradation. The direct approach exhibits high accuracy. However, the indirect approach may lose accuracy due to numerical approximation of derivatives of material-related quantities. The numerical experiments reveal that mesh refinement, especially in the angular direction (θ) around a crack tip, substantially improves accuracy. We recommend that at least sixteen sectors (S16) of singular crack-tip elements be used with the indirect approach, and 12 sectors (S12) with the direct approach. In both approaches, 4 rings (R4) of elements around the crack-tip suffice.

A discussion on the practical usefulness of the present methodology is in order. A potential advantage of the computational fracture scheme developed here is its connection with fracture experiments on both monolithic (uniform composition) and FGM specimens (e.g. initiation toughness and R-curve). For instance, prior to a fracture experiment, a parametric study can be conducted *to investigate the influence of the scale of the property gradation on the energy release rate or* SIFs. This investigation can guide the type and quantity of experiments to be performed, and it is especially important for FGMs due to the potential high cost of such materials (e.g. ceramic FGMs [66] or metal/ceramic FGMs [67]). More specifically, the computational scheme developed here can be used in conjunction with experimental work such as the single edge notched bend (SENB) specimen tests done by Lin *et al.* [68] and by Marur and Tippur [26]. The former deals with mode I fracture (crack face parallel to material gradation) in aluminium alloy 2124/SiC FGMs, and the latter deals with mixed-mode fracture (crack perpendicular to material gradation) in epoxy graded with uncoated solid glass sphere

fillers. For instance, in a previous paper in this journal [23], we have compared Marur and Tippur's [26] experimental/numerical results with our numerical results for K_{I}, K_{II}, and the mixed-mode parameter $\psi = \tan^{-1}(K_{\mathrm{II}}/K_{\mathrm{I}})$. Moreover, carefully designed experiments can also be used to calibrate the parameters used in the computations by providing some of the critical values of material properties, e.g. toughness function, which can be used for crack propagation simulation.

This work offers room for potential extensions to self-adaptive analysis and three-dimensional (3D) fracture mechanics. The self-adaptive mesh-refinement can lead to a systematic selection of the (near-) optimal crack-tip mesh, and also to the mesh transition away from the crack-tip (see, for example, Figures 14 and 15). This *h*-refinement study can build upon the techniques presented by Paulino *et al.* [69]. Finally, the 3D investigation allows assessment of the thickness effect with respect to crack depth and the variation of SIFs throughout a crack front, which are not detectable in two-dimensional problems.

APPENDIX A. DERIVATIVES OF AUXILIARY STRAIN FIELDS DUE TO THE INCOMPATIBILITY TERMS

The auxiliary stress fields with respect to the global co-ordinates are given as

$$\begin{aligned}
\sigma^{\mathrm{g}}_{11}(r,\theta) &= \cos^2\omega(\sigma^{\mathrm{l}}_{11}(r,\theta))^2 + \sin^2\omega(\sigma^{\mathrm{l}}_{22}(r,\theta))^2 - \sin(2\omega)\sigma^{\mathrm{l}}_{12}(r,\theta)\\
\sigma^{\mathrm{g}}_{22}(r,\theta) &= \sin^2\omega(\sigma^{\mathrm{l}}_{11}(r,\theta))^2 + \cos^2\omega(\sigma^{\mathrm{l}}_{22}(r,\theta))^2 + \sin(2\omega)\sigma^{\mathrm{l}}_{12}(r,\theta)\\
\sigma^{\mathrm{g}}_{12}(r,\theta) &= (\cos^2\omega - \sin^2\omega)\sigma^{\mathrm{l}}_{12}(r,\theta) + \sin\omega\cos\omega(\sigma^{\mathrm{l}}_{22}(r,\theta) - \sigma^{\mathrm{l}}_{11}(r,\theta))
\end{aligned} \tag{A1}$$

where $(\cdot)^{\mathrm{g}}$ and $(\cdot)^{\mathrm{l}}$ denote the global and local co-ordinates, respectively, and ω denotes the angle of local co-ordinates with respect to the global co-ordinates, as shown in Figure 1. Using the relationship between stresses and strains, one obtains the auxiliary strain fields with respect to the global co-ordinates as

$$\varepsilon^{\mathrm{g}}_{ij}(r,\theta) = S_{ijpq}(\mathbf{X})\sigma^{\mathrm{g}}_{pq}(r,\theta) \tag{A2}$$

The derivatives of the auxiliary strain fields can be evaluated with respect to the global co-ordinates as follows ($k = 1, 2$):

$$\varepsilon^{\mathrm{g}}_{ij,k} = \frac{\partial\varepsilon^{\mathrm{g}}_{ij}}{\partial X_k} = \frac{\partial\varepsilon^{\mathrm{g}}_{ij}}{\partial r}\frac{\partial r}{\partial X_k} + \frac{\partial\varepsilon^{\mathrm{g}}_{ij}}{\partial\theta}\frac{\partial\theta}{\partial X_k} \tag{A3}$$

where

$$\frac{\partial r}{\partial X_k} = \frac{\partial r}{\partial x_1}\frac{\partial x_1}{\partial X_k} + \frac{\partial r}{\partial x_2}\frac{\partial x_2}{\partial X_k} \tag{A4}$$

and

$$\frac{\partial\theta}{\partial X_k} = \frac{\partial\theta}{\partial x_1}\frac{\partial x_1}{\partial X_k} + \frac{\partial\theta}{\partial x_2}\frac{\partial x_2}{\partial X_k} \tag{A5}$$

with

$$\frac{\partial r}{\partial x_1} = \cos\theta, \quad \frac{\partial r}{\partial x_2} = \sin\theta$$
$$\frac{\partial \theta}{\partial x_1} = \frac{-\sin\theta}{r}, \quad \frac{\partial \theta}{\partial x_2} = \frac{\cos\theta}{r} \tag{A6}$$

ACKNOWLEDGEMENTS

We gratefully acknowledge the support from NASA-Ames, Engineering for Complex Systems Program, and the NASA-Ames Chief Engineer (Dr. Tina Panontin) through grant NAG 2-1424. We also acknowledge additional support from the National Science Foundation (NSF) under grant CMS-0115954 (Mechanics & Materials Program).

REFERENCES

1. Yau JF, Wang SS, Corten HT. A mixed-mode crack analysis of isotropic solids using conservation laws of elasticity. *Journal of Applied Mechanics* (ASME) 1980; **47**(2):335–341.
2. Wang SS, Corten HT, Yau JF. Mixed-mode crack analysis of rectilinear anisotropic solids using conservation laws of elasticity. *International Journal of Fracture* 1980; **16**(3):247–259.
3. Yau JF. Mixed-mode fracture analysis using a conservation integral. *PhD Thesis*, Department of Theoretical and Applied Mechanics, University of Illinois at Urbana-Champaign, 1979.
4. Moës N, Gravouil A, Belytschko T. Non-planar 3D crack growth by the extended finite element and level sets—Part I: mechanical model. *International Journal for Numerical Methods in Engineering* 2002; **53**(11): 2549–2568.
5. Gosz M, Moran B. An interaction energy integral method for computation of mixed-mode stress intensity factors along non-planar crack fronts in three dimensions. *Engineering Fracture Mechanics* 2002; **69**(3):299–319.
6. Nakamura T. Three-dimensional stress fields of elastic interface cracks. *Journal of Applied Mechanics* 1991; **58**(4):939–946.
7. Gosz M, Dolbow J, Moran B. Domain integral formulation for stress intensity factor computation along curved three-dimensional interface cracks. *International Journal of Solids and Structures* 1998; **35**(9–10):1763–1783.
8. Dolbow J, Moës N, Belytschko T. Modeling fracture in Mindlin–Reissner plates with the extended finite element method. *International Journal of Solids and Structures* 2000; **37**(48–50):7161–7183.
9. Dolbow J, Gosz M. On the computation of mixed-mode stress intensity factors in functionally graded materials. *International Journal of Solids and Structures* 2002; **39**(9):2557–2574.
10. Rao BN, Rahman S. Mesh-free analysis of cracks in isotropic functionally graded materials. *Engineering Fracture Mechanics* 2003; **70**(1):1–27.
11. Erdogan F. Fracture mechanics of functionally graded materials. *Journal of Composite Engineering* 1995; **5**(7):753–770.
12. Noda N. Thermal stresses in functionally graded materials. *Journal of Thermal Stresses* 1999; **22**(7):477–512.
13. Paulino GH, Jin ZH, Dodds RH. Failure of functionally grade materials. In *Comprehensive Structural Integrity*, vol. 2, Karihaloo B, Knauss WG (eds). Elsevier Science: Amsterdam, 2002 (Chapter 13).
14. Delale F, Erdogan F. The crack problem for a nonhomogeneous plane. *Journal of Applied Mechanics* (ASME) 1983; **50**(3):609–614.
15. Erdogan F, Wu BH. The surface crack problem for a plate with functionally graded properties. *Journal of Applied Mechanics* (ASME) 1997; **64**(3):449–456.
16. Chan YS, Paulino GH, Fannjiang AC. The crack problem for nonhomogeneous materials under antiplane shear loading—A displacement based formulation. *International Journal of Solids and Structures* 2001; **38**(17): 2989–3005.
17. Delale F, Erdogan F. On the mechanical modeling of an interfacial region in bonded half-planes. *Journal of Applied Mechanics* (ASME) 1988; **55**(2):317–324.
18. Gu P, Asaro RJ. Cracks in functionally graded materials. *International Journal of Solids and Structures* 1997; **34**(1):1–17.

19. Shbeeb NI, Binienda WK, Kreider KL. Analysis of the driving forces for multiple cracks in an infinite nonhomogeneous plate, Part I: Theoretical Analysis. *Journal of Applied Mechanics* (ASME) 1999; **66**(2): 492–500.
20. Shbeeb NI, Binienda WK, Kreider KL. Analysis of the driving forces for multiple cracks in an infinite non-homogeneous plate, Part II: Numerical Solutions. *Journal of Applied Mechanics* (ASME) 1999; **66**(2):501–506.
21. Honein T, Herrmann G. Conservation laws in nonhomogeneous plane elastostatics. *Journal of the Mechanics and Physics of Solids* 1997; **45**(5):789–805.
22. Eischen JW. Fracture of nonhomogeneous materials. *International Journal of Fracture* 1987; **34**(1):3–22.
23. Kim JH, Paulino GH. Finite element evaluation of mixed mode stress intensity factors in functionally graded materials. *International Journal for Numerical Methods in Engineering* 2002; **53**(8):1903–1935.
24. Gu P, Dao M, Asaro RJ. A simplified method for calculating the crack-tip field of functionally graded materials using the domain integral. *Journal of Applied Mechanics* (ASME) 1999; **66**(1):101–108.
25. Anlas G, Santare MH, Lambros J. Numerical calculation of stress intensity factors in functionally graded materials. *International Journal of Fracture* 2000; **104**(2):131–143.
26. Marur PR, Tippur HV. Numerical analysis of crack-tip fields in functionally graded materials with a crack normal to the elastic gradient. *International Journal of Solids and Structures* 2000; **37**(38):5353–5370.
27. Bao G, Cai H. Delamination cracking in functionally graded coating/metal substrate systems. *Acta Mechanica* 1997;**45**(3):1055–1066.
28. Bao G, Wang L. Multiple cracking in functionally graded ceramic/metal coatings. *International Journal of Solids and Structures* 1995; **32**(19):2853–2871.
29. Nemat-Nasser S, Hori M. Micromechanics: overall properties of heterogeneous materials. *North-Holland Series in Applied Mathematics and Mechanics*. North-Holland: The Netherlands, 1993.
30. Kalamkarov AL, Kolpakov AG. *Analysis*, *Design and Optimization of Composite Structures*. Wiley: Chichester, 1997.
31. Aboudi J, Pindera MJ, Arnold SM. Higher-order theory for functionally graded materials. *Composites Part B: Engineering* 1999; **30**(8):777–832.
32. Ostoja-Starzewski M, Jasiuk I, Wang W, Alzebdeh K. Composites with functionally graded interphases: mesocontinuum concept and effective transverse conductivity. *Acta Materialia* 1996; **44**(5):2057–2066.
33. Li JY. Thermoelastic behaviour of composites with functionally graded interphase: a multi-inclusion model. *International Journal of Solids and Structures* 2000; **37**(39):5579–5597.
34. Zuiker JR, Dvorak GJ. The effective properties of functionally graded composites: I. Extension of the Mori–Tanaka method to linearly varying fields. *Journal of Composite Engineering* 1994; **4**(1):19–35.
35. Reiter T, Dvorak GJ, Tvergaard V. Micromechanical models for graded composite materials. *Journal of the Mechanics and Physics of Solids* 1997; **45**(8):1281–1302.
36. Reiter T, Dvorak GJ. Micromechanical models for graded composite materials: II. Thermomechanical loading. *Journal of the Mechanics and Physics of Solids* 1998; **46**(9):1655–1673.
37. Dvorak GJ, Srinivas MV. New estimates of overall properties of heterogeneous solids. *Journal of the Mechanics and Physics of Solids* 1999; **47**(4):899–920.
38. Mori T, Tanaka K. Average stress in matrix and average elastic energy of materials with misfitting inclusions. *Acta Materialia* 1973; **21**(5):571–574.
39. Hill R. A self-consistent mechanics of composite materials. *Journal of the Mechanics and Physics of Solids* 1965; **13**(4):213–222.
40. Christensen RM, Lo KH. Solutions for effective shear properties in three phase sphere and cylinder models. *Journal of the Mechanics and Physics of Solids* 1979; **27**(4):315–330.
41. Jin ZH, Noda N. Crack tip singular fields in nonhomogeneous materials. *Journal of Applied Mechanics* (ASME) 1994; **61**(3):738–740.
42. Williams ML. On the stress distribution at the base of a stationary crack. *Journal of Applied Mechanics* (ASME) 1957; **24**(1):109–114.
43. Parameswaran V, Shukla A. Asymptotic stress fields for stationary cracks along the gradient in functionally graded materials. *Journal of Applied Mechanics* (ASME) 2002; **69**(3):240–243.
44. Eftis J, Subramonian N, Liebowitz H. Crack border stress and displacement equations revisited. *Engineering Fracture Mechanics* 1977; **9**(1):189–210.
45. Kim JH, Paulino GH. Consistent formulations of the interaction integral method for fracture of functionally graded materials. submitted for publication.
46. Knowles JK, Sternberg E. On a class of conservation laws in linearized and finite elastostatics. *Archive for Rational Mechanics and Analysis* 1972; **44**(2):187–211.
47. Budiansky B, Rice JR. Conservation laws and energy-release rates. *Journal of Applied Mechanics* (ASME) 1973; **40**(1):201–203.
48. Kanninen MF, Popelar CH. *Advanced Fracture Mechanics*. Oxford University Press: New York, 1985.
49. Rice JR. Path-independent integral and the approximate analysis of strain concentration by notches and cracks. *Journal of Applied Mechanics* (ASME) 1968; **35**(2):379–386.

50. Raju IS, Shivakumar KN. An equivalent domain integral method in the two-dimensional analysis of mixed mode crack problems. *Engineering Fracture Mechanics* 1990; **37**(4):707–725.
51. Anderson TL. *Fracture Mechanics: Fundamentals and Applications*. CRC Press LLC: Boca Raton, 1995.
52. Kim JH, Paulino GH. Mixed-mode J-integral formulation and implementation using graded finite elements for fracture analysis of nonhomogeneous orthotropic materials: *Mechanics of Materials* 2003; **35**(1–2):107–128.
53. Ma X, Tanihata K, Miyamoto Y, Kumakawa A, Nagata S, Yamada T, Hirano T. Fabrication of TiC/Ni functionally gradient materials and their mechanical and thermal properties. In *Ceramic Engineering & Science Proceedings*, vol. 13. Westerville, Ohio, The American Ceramic Society, 1992; 356–364.
54. Zuiker JR. Functionally graded materials: choice of micromechanics model and limitations in property variation. *Journal of Composite Engineering* 1995; **5**(7):807–819.
55. Hershey AV. The elasticity of an isotropic aggregate of anisotropic cubic crystals. *Journal of Applied Mechanics* (ASME) 1954; **21**(2):236–240.
56. Budiansky B. On the elastic moduli of some heterogeneous materials. *Journal of the Mechanics and Physics of Solids* 1965; **13**(4):223–227.
57. Hill R. Continuum micro-mechanics of elastic-plastic polycrystals. *Journal of the Mechanics and Physics of Solids* 1965; **13**(2):89–101.
58. Hashin Z, Shtrikman S. A variational approach to the theory of the elastic behaviour of multiphase materials. *Journal of the Mechanics and Physics of Solids* 1963; **11**(2):127–140.
59. Wawrzynek PA. Interactive finite element analysis of fracture processes: an integrated approach. *M.S. Thesis*, Cornell University, 1987.
60. Wawrzynek PA, Ingraffea AR. Discrete modeling of crack propagation: theoretical aspects and implementation issues in two and three dimensions. *Report 91-5*, School of Civil Engineering and Environmemtal Engineering, Cornell University, 1991.
61. Santare MH, and Lambros J. Use of graded finite elements to model the behaviour of nonhomogeneous materials. *Journal of Applied Mechanics* (ASME) 2000; **67**(4):819–822.
62. Kim JH, Paulino GH. Isoparametric graded finite elements for nonhomogeneous isotropic and orthotropic materials. *Journal of Applied Mechanics* (ASME) 2002; **69**(4):502–514.
63. Konda N, Erdogan F. The mixed mode crack problem in a nonhomogeneous elastic medium. *Engineering Fracture Mechanics* 1994; **47**(4):533–545.
64. Dong Z, Paulino GH. The mixed-mode crack problem in a finite nonhomogeneous elastic medium under various boundary conditions. in preparation.
65. Kim JH, Paulino GH. Mixed-mode fracture of orthotropic functionally graded materials using finite elements and the modified crack closure method. *Engineering Fracture Mechanics* 2002; **69**(14–16):1557–1586.
66. Carrillo-Heian EM, Carpenter RD, Paulino GH, Gibeling JC, Munir ZA. Densed layered $MoSi_2$/SiC functionally graded composites formed by field activated synthesis. *Journal of the American Ceramic Society* 2001; **84**(5):962–968.
67. Carpenter RD, Paulino GH, Munir ZA, Gibeling JC. A novel technique to generate sharp cracks in metal/ceramic functionally graded materials by reverse 4-point bending. *Scripta Materialia* 2000; **43**(6):547–552.
68. Lin CY, McShane HB, Rawlings RD. Structure and properties of functionally gradient aluminium alloy 2124/SiC composites. *Materials Science and Technology* 1994; **10**(7):659–664.
69. Paulino GH, Menezes IFM, Cavalcante Neto JB, Martha LF. A methodology for adaptive finite element analysis: Towards an integrated computational environment. *Computational Mechanics* 1999; **23**(5–6):361–388.

